Icarus 399 (2023) 115556

Contents lists available at ScienceDirect

Icarus

journal homepage: www.elsevier.com/locate/icarus

Update on SO_2, detection of OCS, CS, CS_2, and SO_3, and upper limits of H_2S and HOCl in the Venus mesosphere using SOIR on board Venus Express

A. Mahieux[a,b,*], S. Robert[a], F.P. Mills[b,c,d], K.L. Jessup[e], L. Trompet[a], S. Aoki[f], A. Piccialli[a], J. Peralta[g], A.C. Vandaele[a]

[a] Royal Belgian Institute for Space Aeronomy, Brussels, Belgium
[b] The University of Texas at Austin, Austin, TX, United States of America
[c] Space Science Institute, Boulder, CO, United States of America
[d] The Australian National University, Canberra, ACT, Australia
[e] South West Research Institute, Boulder, CO, United States of America
[f] The University of Tokyo, Tokyo, Japan
[g] Universidad de Sevilla, Sevilla, Spain

ARTICLE INFO

Keywords:
Venus
Mesosphere
Infrared spectroscopy
Sulfur species

ABSTRACT

We report on the update of SO_2 and first detections of SO_3, CS, and CS_2, and detection of OCS above the cloud deck using the SOIR instrument on-board Venus Express, and upper limit profiles of H_2S and HOCl. Based on the solar occultation spectra measured by SOIR covering all latitudes over the 2006–2014 period, we find an average SO_2 volume mixing ratio of ~0.02 ppm below 90 km which increases to 5 ppm at 100 km; average OCS abundance of 1 ppb to 1 ppm between 65 and 100 km increasing with altitude; mean SO_3 values of 0.1 ppm at 75 km, 1 ppm at 85 km, and 10 ppm at 95 km; CS volume mixing ratios varying from 0.1 ppm at 65 km to 40 ppm at 100 km; finally we report 0.03 ppm of CS_2 at 70 km and 5 ppm at 90 km. It is important to note the detections for all of these species may be biased to higher volume mixing ratios at higher altitudes based on the detection limits for SOIR. Upper-limits for H_2S and HOCl are determined. All abundances show large variabilities with time and/or latitude equal to at least one order of magnitude at all altitudes. We also study the detection statistics of all detected species as a function of time, latitude, and side of the terminator.

1. Introduction

Sulfur chemistry in the Venus mesosphere is one of the two main chemical cycles in and above the cloud layer, together with the carbon cycle. While it involves numerous minor species through photodissociation and recombination reactions such as H_2SO_4, SO_2, SO_3, SO, OCS, HCl, HOCl, H_2O, etc., few of them have been firmly detected above the cloud layer, and their concentrations are only constrained by photochemical models. This work aims to lever these missing pieces of information by providing the first mesospheric vertical profiles of OCS, SO_3, CS, and CS_2, an update of the SO_2 profiles previously published by Mahieux et al. (2015b) and Belyaev et al. (2012), and upper limit detections of H_2S and HOCl. The HCl and H_2O profiles from SOIR previously published in Mahieux et al. (2015d) and Chamberlain et al. (2020) have not changed in the new retrievals.

Multiple measurements of sulfur dioxide (SO_2) above, within, and below the cloud top have been obtained over the past five decades (Vandaele et al., 2017a; Vandaele et al., 2017b). The first cloud-level SO_2 gas detections were reported by ground-based observations in the UV (Barker, 1979). Additional SO_2 detections were then made within and below the Venus clouds by the Pioneer Venus probe in 1978 (Esposito et al., 1997; Esposito et al., 1988) and Venera-15 in 1983 (Moroz et al., 1990; Zasova et al., 1993). Later, the SPICAV-UV instrument on *Venus Express* (VEx) provided decadal monitoring of Venus's above cloud level SO_2 abundance based on solar occultation (Belyaev et al., 2017; Mahieux et al., 2015b), stellar occultation (Evdokimova et al., 2021), and nadir viewing observations (Marcq et al., 2013; Marcq et al., 2020). The SPICAV-UV/VEx solar and stellar occultation observations provide an SO_2 database between 85 and 100 km at the terminator and on the night side, respectively. Large variability and a significant increase of the SO_2 volume mixing ratio (VMR) with increasing altitude are observed at each local solar time observed. A

---

* Corresponding author at: Royal Belgian Institute for Space Aeronomy, Brussels, Belgium.
E-mail address: arnaud.mahieux@aeronomie.be (A. Mahieux).

https://doi.org/10.1016/j.icarus.2023.115556
Received 5 October 2022; Received in revised form 27 March 2023; Accepted 28 March 2023

possible long-term time variation of the SO_2 content at the cloud top (60–65 km) is inferred from the nadir-viewing data, confirming an idea that was proposed after the Pioneer Venus mission (Esposito et al., 1988). Detections made by the VIRTIS/VEx instrument show latitudinal and local solar time dependence of SO_2 at the cloud top (Marcq et al., 2008). SO_2 was also derived from VeRa/VEx X-band radio-occultations - though only below the cloud top in the 51–54 km altitude region, exhibiting not only a clear latitudinal dependence but also a temporal variation at polar latitudes with its abundance at equatorial latitudes kept nearly constant during the VEx mission (Oschlisniok et al., 2021). Ground-based observations in the sub-mm region sounded the altitude region between 70 and 100 km (Sandor et al., 2010) and were able to retrieve SO_2 and SO in two layers, below and above 84 ± 2 km. They found that mixing ratios in the upper layer were nearly a factor of ten larger than in the lower layer. Encrenaz et al. (2015) and Piccialli et al. (2017) reported similar vertical variations and also found spatial variations in SO_2 in the upper mesosphere, above ~80 km, based on ALMA observations. Encrenaz et al. (2012) and Encrenaz et al. (2016) report detections of SO_2 in the upper cloud using TEXES and discuss its spatial distribution. Hubble Space Telescope observations during the VEx era confirm the SOIR cloud top detections at the time (Jessup et al., 2015). Most of these observations are summarized, compared, and thoroughly discussed in two review papers (Vandaele et al., 2017a; Vandaele et al., 2017b).

Regarding the other sulfur compounds, Krasnopolsky (2008) and Krasnopolsky (2010) report the only confirmed OCS measurement available in the upper clouds (~ 65–70 km), and the reported values are significantly larger than the upper limit and potential detection of OCS reported by Sonnabend et al. (2005). Krasnopolsky (2008) gives the lowest upper limit detections for H_2S; no positive detection of SO_3 could be found in the literature; an upper limit on CS_2 is provided by Baker (1978); neither upper limits nor detections for CS and HOCl are reported in the literature. H_2SO_4 and SO are not discussed in this work since they do not have detectable infrared (IR) signatures.

Sulfur compounds probably originate from past and maybe present volcanic activity, which liberated a large amount of sulfur in the atmosphere. The primary gas-phase reservoir for sulfur in the current atmosphere is SO_2 below ~48 km while the primary condensed-phase reservoir is the very thick cloud deck found between ~48 and 70 km, where aerosol droplets are found as a mixture of H_2SO_4 and water. Hazes are found above that altitude, with particles having the same characteristics as the ones found in the main cloud layer, and presenting a large variability (Wilquet et al., 2012). SO_2 above the clouds is photolyzed by the solar UV, producing SO, S, O, and O_2 molecules, which then react in oxidation processes to form SO_3, and are hydrated to form H_2SO_4. Reduced sulfur chemistry on Venus has received limited attention in middle atmosphere chemistry modeling studies. Depending on the local oxidation state, modeled OCS and H_2S are either oxidized via SO_2 and SO_3 to H_2SO_4 or reduced to polysulfur, S_x, both of which can condense to form aerosol particles, as they are transported upward through the cloud layers (e.g., Bierson and Zhang (2020); Krasnopolsky (2016); Marcq et al. (2018); Prinn (1975)). Neither OCS nor H_2S is sufficiently abundant to dominate sulfur chemistry on Venus, but OCS and H_2S were studied most recently in connection with potential PH_3 chemistry on Venus (Bains et al., 2021). Observations and models (Bierson and Zhang, 2020; Krasnopolsky, 2012; Mills and Allen, 2007; Zhang et al., 2012) agree that the OCS mixing ratio decreases rapidly with increasing altitude through the upper cloud as OCS photolyzes and reacts with S and that the vertical profile for OCS is very sensitive to the eddy diffusion profile through the upper cloud. CS and CS_2 do not appear to have been included in any Venus atmospheric chemistry model to date. They are included in terrestrial and exoplanet models studying sulfur fractionation in the Archean, the terrestrial sulfur cycle, polymerization to form organic compounds and hazes; and potential biosignatures (e.g., Colman et al. (1996); Domagal-Goldman et al. (2011); Kettle et al. (2002); Lyons (2009)). CS and CS_2 were also important in models developed to understand the Shoemaker-Levy 9 impact on Jupiter (Moses et al., 1995). HOCl has been included in some recent Venus middle atmosphere photochemical models (e.g., Bains et al. (2021); Pinto et al. (2021); Zhang et al. (2012)), but its chemistry has not been analyzed. In the Pinto et al. (2021) simulation with 3 ppm SO_2 at 58 km, HOCl is predominantly formed via $ClO + HO_2 \rightarrow HOCl + O_2$ but this reaction is a very minor loss channel for both ClO and HO_2. HOCl is predominantly destroyed via Cl + HOCl and secondarily via photolysis. These reactions are a minor source for Cl and very minor sources for OH, Cl, Cl_2, and HCl.

In the following, we first describe the SOIR instrument and the measurement technique in section 2. We then provide a summary of the retrieval procedure and its application to retrievals in section 3. The results are presented in section 4 and discussed in section 5. Finally, the conclusion is given in section 5.

2. The observations

2.1. The SOIR instrument

SOIR (Nevejans et al., 2006) was an infrared spectrometer on board VEx. The scientific phase of the VEx mission started in June 2006 and ended in December 2014. SOIR was operating exclusively in solar occultation mode and was thus only taking measurements at the Venus terminator (6 AM or 6 PM), covering all latitudes from Pole to Pole. VEx had a polar elliptical orbit, with the perigee located a few hundred kilometers above the North Pole, and the apogee at altitudes varying between 45,000 and 65,000 km above the South Pole.

SOIR combined an echelle grating for light diffraction with an Acousto Optic Tunable Filter (AOTF) for order sorting (Mahieux et al., 2008). The instrument was working at very high diffraction orders (101 to 194), simply called orders in the following, covering the 2.2 to 4.4 μm region, or 2200 to 4400 cm^{-1}. The detector counted 320 pixel rows along its spectral direction and 24 illuminated pixel columns in its spatial direction. Because of telemetry limitations, the spatial columns had to be binned on board into two spatial bins. When projected at the tangent point in the atmosphere, the two spatial bins are superimposed in the vertical direction; they thus correspond to two slightly different tangent altitudes. SOIR could record spectra in four orders during an occultation, at a 1 Hz cadence. Therefore, each solar occultation counted eight independent series of spectra (two bins × four orders).

The SOIR transmittance spectra were obtained by dividing the spectra measured while the instrument line of sight was crossing the Venus atmosphere (with tangent altitudes ranging from 60 to 200 km) by spectra free of any atmosphere contribution taken before or after the occultation (with tangent altitudes above 220 km, with at least 20 spectra, usually >100 spectra). The procedure to construct the transmittance spectra and their associated uncertainties is described in Trompet et al. (2016) and Mahieux et al. (2010): solar occultation transmittance spectra are self-calibrated in terms of signal intensity since they are obtained by computing the ratio of two spectra measured by SOIR. Only the pixel and order to wavenumber calibration need to be adjusted for each spectrum and are modeled as a fourth-order polynomial. We note that the pointing of the satellite was stable enough (with pointing errors of the order of 0.2 mrad) such that projected instrument slit was always within the Sun disk.

The instrument spectral resolution varied from 0.11 to 0.21 cm^{-1} and the spectral width of a pixel from 0.06 to 0.12 cm^{-1}, both with increasing ascending orders. The AOTF bandpass function had a shape close to a $sinc^2$, with a full width at half-maximum (FWHM) equal to 24 cm^{-1} (Mahieux et al., 2009). Because the AOTF FWHM was of the same order of magnitude as the instrument free spectral range (~24 cm^{-1}), the spectra recorded in a given order experienced leakage from the adjacent orders. For this reason, when constructing an analytical SOIR spectrum, the contribution from seven orders is considered (the targeted order and the three orders just above and below). This implies that absorption lines seen in a spectrum can come from adjacent orders. Such a procedure is described in Mahieux et al. (2009). A second-order polynomial provides a correspondence between the wavenumber position of the maximum of the AOTF bandpass and the radio-frequency (RF) applied to the AOTF crystal (Mahieux et al., 2008). The typical signal-to-noise ratio (SNR) varied between 500 and 3000 (Vandaele et al., 2013).

The vertical sampling, which corresponds to the vertical distance between two observations for a given order and bin varied between 2 km at the North Pole, 500 m between 40° and 70° North and up to 5 km at the South Pole, due to the elliptical orbit of the spacecraft. The vertical resolution, which is the size of the projected instrument slit at the measurement point since the Sun covers the whole detector during the measurements (Mahieux et al., 2008), was also latitude dependent; it ranged from 200 m for Northern polar observations to 5 km at the South Pole.

2.2. *Spectroscopy*

The seven species targeted in this study are all close to the SOIR detection limit when considering typical expected VMRs based on the literature when possible. We only consider the main isotopologue of each species. The position and intensity of the targeted lines are summarized in Fig. 1, where the line intensities are multiplied by typical VMRs expected above the cloud top. The orders in which SO_2, OCS, SO_3, H_2S, HOCl, CS, and CS_2 absorb are listed in Table 1.

We note that the OCS bands around 2550, 3100, and 3950 cm^{-1}, the CS_2 bands around 2300 and 2950 cm^{-1}, the H_2S band around 2400 cm^{-1} and the left side of the band at 3700 cm^{-1} were not considered in this study, because they are located below much stronger bands of other species, and would not return any positive detection.

Table 1

List of the orders used to retrieve the targeted species. The wavenumber range of each order is provided, with the vibrational transition in HITRAN notation, and the list of the other species simulated in each order.

Order	Wavenumber range [cm^{-1}]	Targeted species	Targeted vibrational transition	Other species absorbing in the order
110	2458.3–2479.4	SO_2	101–000	CO_2
111	2480.6–2502.0	SO_2 CS	101–000 2–0	CO_2
112	2503.0–2524.5	SO_2 CS	101–000 2–0	CO_2
113	2525.3–2547.0	CS	2–0	CO_2
119	2659.4–2682.3	H_2S	100–000	CO_2, HDO, HCl
120	2681.8–2704.8	H_2S	100–000	CO_2, HDO, HCl
121	2704.1–2727.4	H_2S	100–000	CO_2, HDO, HCl
124	2771.2–2795.0	SO_3	002200E'-000000A1'	CO_2, HDO, HCl
125	2793.5–2817.5	SO_3	002200E'-000000A1'	CO_2, HDO, HCl
126	2815.9–2840.1	CS_2	2001–0000	HDO, HCl
127	2838.2–2862.6	CS_2	2001–0000	CO_2, HDO, HCl
128	2860.6–2885.1	OCS	1001–0000	CO_2, HDO, HCl
129	2882.9–2907.7	OCS	1001–0000	HDO, HCl
130	2905.3–2930.2	OCS	1001–0000	HDO, HCl
131	2927.6–2952.8	OCS	1001–0000	HDO, HCl
168	3754.5–3786.7	HOCl	100–000	CO_2, H_2O
169	3776.8–3809.3	H_2S	011–000	CO_2, H_2O
170	3799.2–3831.8	H_2S	011–000	CO_2, H_2O, HF
171	3821.5–3854.4	H_2S	011–000	CO_2, H_2O, HDO, HF
172	3843.9–3876.9	H_2S	011–000	CO_2, H_2O, HF
173	3866.2–3899.4	H_2S	011–000	CO_2, H_2O, HF
182	4067.4–4102.3	OCS	0002–0000	CO_2, H_2O, HF, CO
183	4089.7–4124.8	OCS	0002–0000	CO_2, H_2O, HF, CO

3. Retrieval algorithm

3.1. *The inversion algorithm*

The inversion algorithm best fits the integrated slant density from each measured transmittance spectrum using the Levenberg-Marquardt (LM) least-square algorithm of MATLAB. More specifically, each transmittance spectrum (obtained at a given tangent height) is fitted by adjusting the integrated slant density of all species absorbing in the diffraction order (listed in columns 3 and 5 of Table 1), the coefficients of the pixel to wavenumber calibration, the wavenumber position of the maximum of the AOTF bandpass function, the instrument spectral resolution, and an atmospheric slant temperature proxy. Indeed, the pixel-to-wavenumber calibration may vary from one measured spectrum to another due to several factors, such as the temperature inside the SOIR

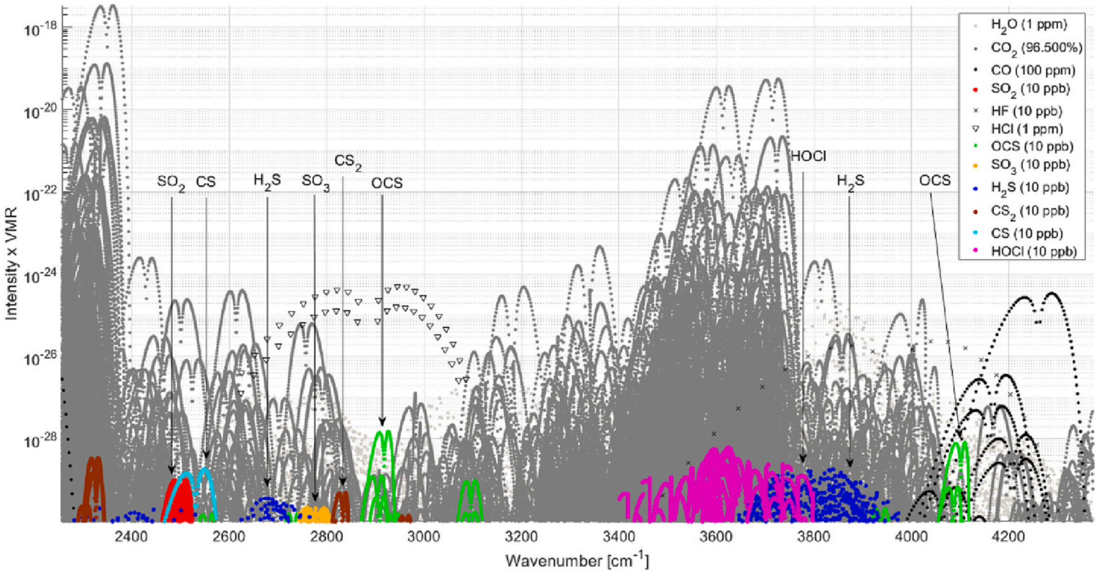

Fig. 1. Position and line intensities multiplied by typical Venus volume mixing ratio (VMR) for the targeted species and the dominant species in the studied spectral range. The typical VMRs are given in the figure caption. The line positions and intensities are from HITRAN (Gordon et al., 2017). The bands used in this study are listed in Table 1.

instrument, which varies by a few degrees during an observation, and due to possible Doppler shifts originating from atmospheric winds. The position of the maximum of the bandpass function and the instrument spectral resolution may also be temperature-dependent (Mahieux et al., 2008). These two quantities are expected to not vary too much during an occultation. We discuss the variation of the calibration parameters in section 3.5. Finally, we adjust an atmospheric slant temperature proxy, since the IR absorption cross sections are temperature dependent. This temperature proxy does not correspond to the atmospheric temperature at the tangent point, since it is adjusted considering the whole slant and not the temperature at the tangent point. The temperature proxy is fitted in the procedure to diminish the reduced-χ^2 between the measured spectrum and the fitted one but is not used further as a result considering it is only a proxy. It represents the temperature along the line of sight weighted by the absorption opacity and thus has no physical meaning. Mahieux et al. (2015c) discuss this matter in section 3.2 of that paper, where CO_2 rotational temperatures are determined from the SOIR CO_2 spectra. We also discuss the influence of the temperature profile in section 3.6 of this paper.

The spectra are processed to first retrieve the slant densities of the different species absorbing in each diffraction order, see Table 1, and in a second step the number densities. Based on several criteria (see section 3.2), detections are pointed out and analyzed further. If the number of detections during an observation is larger than 1, we then use the Tikhonov regularization method (Doicu et al., 2010) to compute the local number densities of the minor species, using the scheme described in Gröller et al. (2018) or Trompet et al. (2022). The value of the λ-parameter of the Tikhonov method is typically set up to 0.1 or 1, the latter being used when stronger smoothing is required. We then compute the VMR by dividing the retrieved number density by the total density, which we obtain from the Venus International Reference Atmosphere (VIRA) model (Keating et al., 1985; Zasova et al., 2006).

We stress that the transmittance measurements should be sensitive to three atmospheric parameters: the species number density, the temperature, and the total pressure. We explained in Mahieux et al. (2010) that the SOIR transmittances are not sensitive to the total pressure: even if the resolution of SOIR ($\sim$0.15 cm^{-1}) is good enough to resolve most of the atmospheric absorption lines, it remains a few factors larger than the width of the pressure broadened atmospheric absorption lines (the typical Full Width at Half Maximum of the atmospheric absorption lines at infinite resolution is of the order of 0.001 cm^{-1}). We then fit the two other parameters, by fitting the number density of the species, and the temperature proxy. The a priori of the temperature proxy is taken as the temperature profiles derived from the CO_2 number density profile measured during each occultation (Mahieux et al., 2015a). Thus, the retrievals developed here are independent of any background atmosphere conditions, which means that we do not need any VIRA information to perform our fits. VIRA is only used when we translate the measured number densities into VMRs.

When computing the uncertainty on the VMR, we only consider the error on the targeted species, and we do not include any error on the total number density from VIRA.

In the terminator region, rapid changes of density and temperature are observed at a given altitude level while varying the solar longitude, i.e. from 5 pm to 7 pm or 5 am to 7 am, as one goes from dayside to nightside or inversely. The impact of such variations on the retrievals were studied by Piccialli et al. (2021) for the case of ozone retrievals on Mars using solar occultations. They show that accounting for such rapid variations in the vertical inversion (1) have rather small impact on the values of the derived vertical profile (they are of the order of the uncertainty on the retrieved local number densities), and (2) can only be accounted for while considering the cross-terminator gradient obtained from Global Climate Models (GCM). Since GCMs do not yet include most of the species detected in this work, we neglect the impact of the cross-terminator variations as it would be outside of the scope of this work.

3.2. Detection criteria

We only consider fits for which the LM algorithm converged to a minimum, of which we consider the fitted integrated slant densities of all the fitted species. In order to confirm a positive detection of the minor species in a spectrum measured in a given order and for a given bin, we use four criteria. A detection is claimed only if all criteria are satisfied for each retrieved integrated slant density:

(a) *Criterion on comparing fits with and without the targeted minor species*: The first criterion relies on comparing the fit of each spectrum with (named S_1) and without (named S_2) the targeted minor species. Practically, we run a second inversion using the method described in section 3.1 considering only the major species listed in column 5 of Table 1, and we compare the reduced-χ^2 of both fits. The reduced-χ^2, which we will name χ_ν^2 in the following, is computed as $\frac{1}{(n-m)}\cdot\sum_{i=1}^{n}\left(\frac{y_{obs,i}-y_{calc,i}}{dy_{obs,i}}\right)^2$, where m is the number of fitted variables, n is the number of spectral points, $y_{obs,\ i}$ is the measured spectrum, $y_{calc,\ i}$ is the synthetic spectrum, and $dy_{obs,\ i}$ is the uncertainty on the measured spectrum. If χ_ν^2 lowers by a given percentage while including the minor species in the fitting procedure, then the criterion is satisfied. In the current study, we consider percentage values of 5, 10, and 20%, similar to what was done by Evdokimova et al. (2021). This criterion is used to ensure that adding the minor species to the fit provides a significantly better agreement between the two fits, i.e. with and without the minor species. A third spectrum is also considered, named S_3, that is built using the same slant densities that were retrieved to build S_1, but setting the targeted minor species slant densities to zero. The same condition is applied on the χ_ν^2 between S_1 and S_3, i.e. a reduction of the χ_ν^2 by the same 5, 10, or 20%, to satisfy this criterion.

(b) *Criterion on the upper detection limit*: We compute the white-noise and detection upper-limit using the same method as the one described in Appendix F of Trompet et al. (2021). The upper detection limit is computed while comparing the noise in the spectra and the absorption cross-section of the targeted gas to compute the minimum number density that could be measured by SOIR, assuming a constant volume mixing ratio profile of the targeted minor species. As explained by Trompet et al. (2021), the strongest line of the targeted minor species in the measured order should be at least between 1 and 3.2 times higher than the noise level to be considered a clear detection. In this work, we consider the values of 1 and 3.2 larger than the noise level. Only slant number densities larger than the white-noise upper limit detection satisfy this criterion. This criterion is typical of this kind of study, where the retrieved densities are compared to the upper limit densities computed only from the noise level, and not the measured spectrum itself.

(c) *Criterion on the correlations between observed and synthetic spectra*: We compute for each spectrum the correlation C_1 between the measured transmittance and the synthetic transmittance considering the minor and major species S_1, and the correlation C_2 between the measured spectrum and the synthetic spectrum considering only the major species S_2. The third criterion is satisfied if $C_1 > C_2$. The same criterion is applied between S_1 and S_3, with S_3 being the spectrum built considering the slant densities retrieved to build S_1, but setting the targeted minor species slant density to 0. In other words, we force $C_1 > C_3$. The correlations are computed using the corrcoeff routine in MATLAB. This criterion is used to show that adding the minor species increases the spectral structure agreement between measured and synthetic fitted spectra.

(d) *Criterion on the uncertainties of the retrieved slant densities*: For each retrieved slant density, we only consider values for which the retrieved slant density is larger than its uncertainty returned by the LM algorithm.

We note that we only consider observed spectra that have a mean transmittance larger than 0.01.

All these criteria are not used on the entire measured spectrum, but rather applied on specific wavenumber regions in each spectrum. The wavenumber regions corresponding to detector pixels between 1 and 100, and between 300 and 320 are discarded because the signal-to-noise ratio is always worse than for the other pixels. Also, for specific orders in which H_2S absorbs, we only apply the criteria in regions where strong lines of that species are found, corresponding to the intervals 2672.2 to 2673.6 cm^{-1}, 2674.6 to 2675.8 cm^{-1}, and 2677.4 to 2679 cm^{-1} for order 119, 2688.8 to 2692 cm^{-1} and 2696.6 to 2699.2 cm^{-1} for order 120, and 2711.2 to 2716.5 cm^{-1} and 2717.2 to 2718.3 cm^{-1} for order 121. For HOCl, we only focus on the region 3766.5 to 3770 cm^{-1} for the same reason. We stress that the fitting procedure described in section 3.1 is done on the whole wavenumber range, only the criteria defined in this section are applied in those spectral regions.

As a summary, we will provide detections based on six detection criteria categories, depending on the reduction of χ_ν^2 while including the minor species in the fit (criterion *a*) by either 5, 10, or 20%, and depending on the comparison with the white-noise or detection upper-limit (criterion *b*), while always satisfying criteria *c* and *d*.

3.3. Retrieval of synthetic spectra

In order to check the robustness of the proposed approach, we built synthetic spectra for each of the orders listed in Table 1, to which we added noise (with SNR values of 500, 1000, 2000, and 3000), and used the algorithm described above to retrieve the densities of the major and minor species. For minor species VMRs of 0.1, 1, and 10 ppm were used in these simulations. We considered two typical altitudes: 80 and 65 km. We checked the quality of the retrievals and we consider the detection criteria described in the previous section considering a reduction of χ_ν^2 by 5% (criterion *a*) and compared to the white-noise upper limit to decide whether a detection was obtained or not. We considered typical observation geometries. The summary of the results is presented in Table 2, while the numerical values of the retrieved VMRs and associated uncertainties are provided in the supplementary material, see Table 5 in Appendix B. The results were obtained considering slant densities for CO_2 of 1.7×10^{24} cm^{-2}, and the species VMRs as in the legend of Fig. 1, and a temperature of 200 K, a pressure of 5.5 mbar and a slant path of 200 km at 80 km; and 1.7×10^{27} cm^{-2} and same VMRs for the other species, a temperature of 230 K, and a pressure of 65 mbar at 65 km.

We see that:

- SO_2 should be detected at both altitudes, for VMRs down to values of at least 0.1 ppm, for all orders and SNRs;
- OCS should also be detectable at both altitudes, for VMRs down to values of at least 0.1 ppm, for all orders and SNRs;
- SO_3 should have positive detections for all VMRs and SNRs at 65 km, and for VMRs larger than 1 ppm for all SNRs at 65 km; VMRs of 0.1 ppm should only be detectable for SNRs larger than 3000;
- HOCl should only be detectable at 80 km for VMRs larger than 1 ppm, and for SNRs larger than 2000 for VMRs of 0.1 ppm; it is not detectable at 65 km;
- H_2S should be detectable for all VMRs and SNRs at 65 km, except for orders 169 and 170; depending on the order and the SNR, H_2S should be detectable down to 0.01 ppm;
- CS should be detectable for all SNRs, VMRs at 65 km, while it is only detectable for VMRs between larger 1 ppm at 80 km depending on the SNR and the order;
- CS_2 should be detectable for all SNRs and VMRs at 65 km, while at 80 km it is detectable only for VMRs larger than 10 ppm in all orders, except order 126 where it is also detectable for VMR of 1 ppm and SNR of 3000.

We note that, in general, there is greater detectability at 65 km than at 80 km. The slant path determines the detectability of the species: lower in the atmosphere there is a higher density of CO_2 and trace gases, and even though high CO_2 leads to lower light transmittances, unless the observed line order is fully saturated (such as in orders 168, 169, and 170, that are within the CO_2 2.7 μm band), it is easier to detect the trace species at lower altitudes where the gas density is highest. In those cases where the detection criteria is not met, an upper limit is defined. Typical examples of upper limit profiles can be found in Fig. 19 for H_2S and HOCl.

These results provide (1) proof of the working principle of the algorithm, and (2) orders of magnitude of detectability for each species, since they were produced considering a hypothetical observation geometry and random noise uniformly distributed across the wavenumber range.

3.4. Example of fits

Examples of fits are provided for all species, except for H_2S and HOCl for which no detection is reported.

3.4.1. Sulfur dioxide

Occultation 341.1, where the decimal value indicates the measurement sequence, was taken on 28 March 2007 on the evening side of the terminator at a latitude of 82°N and longitude of 348°W. We focus on the spectrum taken at a tangent altitude of 71.2 km in order 112, bin #2. This order records the absorption structures of CO_2, CS, and SO_2. CS is discussed in section 3.4.4, and it was not positively detected in this particular spectrum. SO_2 was detected under the conditions described in section 3.2, and an example of spectrum is plotted in Fig. 2, where the measured spectrum, the best fit of the major and minor species (Simulation S_1, considering $CO_2 + CS + SO_2$) synthetic spectrum, the best fit of the major species only and non targeted minor species (Simulation S_2, considering $CO_2 + CS$) synthetic spectrum, and the best fit of the major and minor species from which the signature of the targeted minor species SO_2 is set to zero (Simulation S_3, considering $(CO_2 + CS + SO_2) - (SO_2)$) are plotted. *M* refers to the measured transmittance, and *dM* to the noise. The black shaded region corresponds to the spectral region that is not considered while using the criteria described in section 3.2. The yellow-shaded regions correspond to spectral regions where $|M - S_1| < |M - S_2|$ and the SO_2 signal is larger than the noise ($|S_1 - S_3| < dM$). In the center panel of the same figure, we provide the noise level, the SO_2 signature (given as $S_1 - S_3$) as the black spectrum, and the residuals of $(M - S_1)$, $(M - S_2)$, and $(M - S_3)$. We note that in most of the spectral regions where SO_2 has a stronger signature, the fit is enhanced. χ_ν^2 and the correlation coefficients between *M*, S_1, S_2, and S_3 are given in the legend of the figure. χ_ν^2 between *M* and S_1 is lower than χ_ν^2 between *M* and S_2 by $1 - \frac{\chi^2_{M-S_1}}{\chi^2_{M-S_2}} = 14.5\%$, and χ_ν^2 between *M* and S_1 is lower than χ_ν^2 between *M* and S_3 by $1 - \frac{\chi^2_{M-S_1}}{\chi^2_{M-S_3}} = 56.73\%$. The correlation of S_1 with *M* is larger than the correlation of S_2 with M by $1 - \frac{corr_{(M,S_2)}}{corr_{(M,S_1)}} = 0.06\%$, and the correlation of S_1 with *M* is larger than the correlation of S_3 with M by $1 - \frac{corr_{(M,S_3)}}{corr_{(M,S_1)}} = 0.1\%$. We note that the relative increase of the correlations is small since both correlations are very close to one.

We also present in the left panels of Fig. 2 histograms of the distributions of the weighted residuals relative to the two fits, $H_{(M-S_1)}$ and $H_{(M-S_2)}$. We fit a Gaussian to each of those, and compute their σ-values $\sigma_{H_{(M-S1)}}$ and $\sigma_{H_{(M-S2)}}$ and the corresponding uncertainties $\delta\sigma_{H_{(M-S1)}}$ and $\delta\sigma_{H_{(M-S2)}}$. We see that the σ_H-values are significantly different by 2σ, since $\sigma_{H_{(M-S1)}} + 2 \cdot \delta\sigma_{H_{(M-S1)}} < \sigma_{H_{(M-S2)}}$ $(3.8477 + \mathbf{2} \cdot 0.1464 < 4.4539)$ and $\sigma_{H_{(M-S2)}}$

Table 2

Detections for a reduction of the fit by 5% (criterion a) for initial concentrations of 0.1, 1, and 10 ppm and SNRs of 500, 1000, 2000, and 3000 for the retrievals of the synthetic spectra in orders where SO_2, OCS, SO_3, H_2S, HOCl, CS, and CS_2 absorb. The first column lists the species, the second column the orders, the third column the initial concentrations used to build the synthetic spectra, and the last four columns the different SNRs for each tangent altitude. Green checks correspond to positive detections while red crosses to non-detections, based on the four criteria from section 3.2.

Species	Order	Initial VMR [ppm]	SNR							
			At 65 km				At 80 km			
			500	1000	2000	3000	500	1000	2000	3000
SO_2	110	0.1	✓	✓	✓	✓	✓	✓	✓	✓
		1	✓	✓	✓	✓	✓	✓	✓	✓
		10	✓	✓	✓	✓	✓	✓	✓	✓
	111	0.1	✓	✓	✓	✓	✓	✓	✓	✓
		1	✓	✓	✓	✓	✓	✓	✓	✓
		10	✓	✓	✓	✓	✓	✓	✓	✓
	112	0.1	✓	✓	✓	✓	✓	✓	✓	✓
		1	✓	✓	✓	✓	✓	✓	✓	✓
		10	✓	✓	✓	✓	✓	✓	✓	✓
OCS	128	0.1	✓	✓	✓	✓	✓	✓	✓	✓
		1	✓	✓	✓	✓	✓	✓	✓	✓
		10	✓	✓	✓	✓	✓	✓	✓	✓
	129	0.1	✓	✓	✓	✓	✓	✓	✓	✓
		1	✓	✓	✓	✓	✓	✓	✓	✓
		10	✓	✓	✓	✓	✓	✓	✓	✓
	130	0.1	✓	✓	✓	✓	✓	✓	✓	✓
		1	✓	✓	✓	✓	✓	✓	✓	✓
		10	✓	✓	✓	✓	✓	✓	✓	✓
	131	0.1	✓	✓	✓	✓	✓	✓	✓	✓
		1	✓	✓	✓	✓	✓	✓	✓	✓
		10	✓	✓	✓	✓	✓	✓	✓	✓
	182	0.1	✓	✓	✓	✓	✓	✓	✓	✓
		1	✓	✓	✓	✓	✓	✓	✓	✓
		10	✓	✓	✓	✓	✓	✓	✓	✓
	183	0.1	✓	✓	✓	✓	✓	✓	✓	✓
		1	✓	✓	✓	✓	✓	✓	✓	✓
		10	✓	✓	✓	✓	✓	✓	✓	✓
SO_3	124	0.1	✓	✓	✓	✓	×	×	×	✓
		1	✓	✓	✓	✓	✓	✓	✓	✓
		10	✓	✓	✓	✓	✓	✓	✓	✓
	125	0.1	✓	✓	✓	✓	×	×	×	✓
		1	✓	✓	✓	✓	✓	✓	✓	✓
		10	✓	✓	✓	✓	✓	✓	✓	✓
HOCl	168	0.1	×	×	×	×	×	×	✓	✓
		1	×	×	×	×	✓	✓	✓	✓
		10	×	×	×	×	✓	✓	✓	✓
H_2S	119	0.1	✓	✓	✓	✓	×	×	×	×
		1	✓	✓	✓	✓	✓	✓	✓	✓
		10	✓	✓	✓	✓	✓	✓	✓	✓
	120	0.1	✓	✓	✓	✓	×	×	×	×
		1	✓	✓	✓	✓	✓	✓	✓	✓
		10	✓	✓	✓	✓	✓	✓	✓	✓
	121	0.1	✓	✓	✓	✓	×	×	×	×
		1	✓	✓	✓	✓	×	✓	✓	✓
		10	✓	✓	✓	✓	✓	✓	✓	✓
	169	0.1	×	×	×	×	×	×	✓	✓
		1	×	×	×	×	✓	✓	✓	✓
		10	×	×	×	×	✓	✓	✓	✓
	170	0.1	×	×	×	×	×	✓	✓	✓
		1	×	×	×	×	✓	✓	✓	✓
		10	×	×	×	×	✓	✓	✓	✓
	171	0.1	✓	✓	✓	✓	×	✓	✓	✓
		1	✓	✓	✓	✓	✓	✓	✓	✓
		10	✓	✓	✓	✓	✓	✓	✓	✓
	172	0.1	✓	✓	✓	✓	×	×	✓	✓
		1	✓	✓	✓	✓	✓	✓	✓	✓
		10	✓	✓	✓	✓	✓	✓	✓	✓
	173	0.1	✓	✓	✓	✓	×	×	✓	✓
		1	✓	✓	✓	✓	✓	✓	✓	✓
		10	✓	✓	✓	✓	✓	✓	✓	✓
CS	111	0.1	✓	✓	✓	✓	×	×	×	×
		1	✓	✓	✓	✓	×	×	×	✓
		10	✓	✓	✓	✓	✓	✓	✓	✓
	112	0.1	✓	✓	✓	✓	×	×	×	×
		1	✓	✓	✓	✓	×	×	✓	✓
		10	✓	✓	✓	✓	✓	✓	✓	✓
	113	0.1	✓	✓	✓	✓	×	×	×	×
		1	✓	✓	✓	✓	×	×	✓	✓

(*continued on next page*)

Table 2 (*continued*)

Species	Order	Initial VMR [ppm]	SNR							
			At 65 km				At 80 km			
			500	1000	2000	3000	500	1000	2000	3000
CS_2		10	✓	✓	✓	✓	✓	✓	✓	✓
	126	0.1	✓	✓	✓	✓	×	×	×	×
		1	✓	✓	✓	✓	×	×	×	✓
		10	✓	✓	✓	✓	✓	✓	✓	✓
	127	0.1	✓	✓	✓	✓	×	×	×	×
		1	✓	✓	✓	✓	×	×	×	×
		10	✓	✓	✓	✓	✓	✓	✓	✓

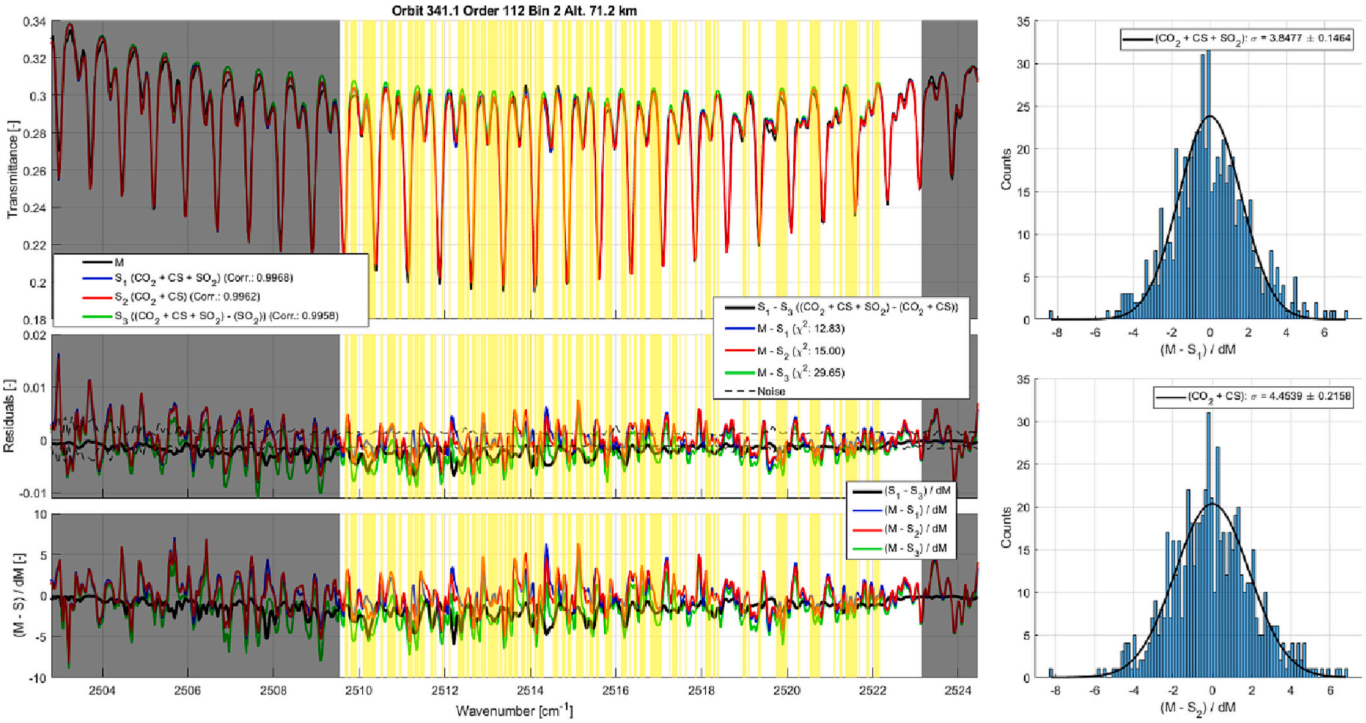

Fig. 2. (Top left panel) Example of SO_2 fit during orbit 341.1 in order 112 bin #2 at a tangent altitude of 71.2 km. The upper panel depicts the measured spectrum (M in black), the synthetic spectrum considering the major and minor species CO_2, SO_2, and CS (S_1 in blue), the synthetic spectrum considering the major species CO_2 only and the non targeted minor species CS (S_2 in red), and the synthetic spectrum considering the major and minor species CO_2, SO_2, and CS from which the signature of the targeted minor species SO_2 is set to zero (S_3, in green). The values of the correlation coefficients between the measured and synthetic spectra are given in the legend. The black-shaded wavenumber regions correspond to the regions that are not used to check the criteria defined in section 3.2. The yellow-shaded regions correspond to regions where the S_1 spectrum better fits the measured spectrum M than S_2 and where the SO_2 signature is larger than the noise. (Center left panel) The noise of the measurement (dashed black lines, dM), SO_2 contribution to the synthetic spectrum in black (S_1 – S_3), residuals between the measured and synthetic spectra with major and minor species in blue (M – S_1), residuals between the measured and synthetic spectra considering the major species only in red (M – S_2), and residuals between the measured and synthetic spectrum considering the major and minor species CO_2, SO_2, and CS from which the signature of the targeted minor species SO_2 is set to zero (M – S_3). The values of χ_ν^2 are given in the legend. (Bottom left panel) Residuals weighted by the noise, which is used to compute the χ_ν^2. (Top right panel) Histogram of the distribution of the residuals weighted by the uncertainties of the major and minor species fit (M – S_1), and fit of the distribution by a Gaussian. (Bottom right) Histogram of the distribution of the residuals weighted by the uncertainties of the major species and the non targeted minor species fit (M – S_2), and fit of the distribution by a Gaussian.

$- 2 \cdot \delta\sigma_{H_{(M\text{-}S2)}} > \sigma_{H_{(M\text{-}S1)}}$ ($4.4539 - \mathbf{2} \cdot 0.2158 > 3.8477$).

The fitted SO_2 integrated slant density is equal to $1.36 \times 10^{18} \pm 2.78 \times 10^{17}$ cm^{-2}, and the upper-limit detection is equal to 1.86×10^{15} cm^{-2}, with a local number density at 69.2 km equal to $2.68 \times 10^{10} \pm 4.83 \times 10^{9}$ cm^{-3}.

However, due to the working principle of the instrument, some lines in this spectrum correspond to the ones absorbing in the targeted order, while others are coming from adjacent orders, all modulated by the AOTF transfer function. The working principles of the instrument, the method to compute the noise value, and the instrument spectral characteristics are described in details in Trompet et al. (2016) and Mahieux et al. (2010).

We see in the example provided in Fig. 2 that the SO_2 spectrum has peaks that are very close to the noise level, exceeding it only by no more than a factor of 2 in some spectral regions. As mentioned above, the yellow shaded boxes show the regions where adding SO_2 to the computation better fits the measured spectrum while the SO_2 signal is larger than the noise. We see that some of the SO_2 lines do not satisfy those criteria (for example at 2512.2 or 2514.4 cm^{-1}), and do better in many others. We recall that detections are claimed based on statistical criteria, rather than systematic line fit since the SO_2 signal is very close to the noise level. Moreover, the list of criteria listed in section 3.2 ensures that the fit is a positive detection, thanks to (1) the χ_ν^2 reduction while considering the minor species in the fit, (2) the retrieved slant density values that are larger than the upper limit slant density values, (3) the increase of correlation between the measured and the fitted spectra while considering the minor species in the fit, and (4) that the retrieved slant density is larger than its associated uncertainty.

3.4.2. *Carbonyl sulfide*

For OCS, we focus on occultation 480.1, taken on 14 August 2007 on the morning side of the terminator at a latitude of 78°N and longitude of 238°W. We consider the spectrum taken at a tangent altitude of 86.2 km in order 131, bin #2, see Fig. 3. In this order, H_2O, HCl, CO_2, and OCS have absorption lines. This detection in this observation shows a larger correlation with M for the fit of S_1 than for S_2 by $1-\frac{corr_{(M,S_2)}}{corr_{(M,S_1)}}=1.55\%$, and a larger correlation with M and S_1 than M and S_3 by $1-\frac{corr_{(M,S_3)}}{corr_{(M,S_1)}}=0.32\%$. We observe a reduction of the χ_ν^2 by $1-\frac{\chi^2_{M-S_1}}{\chi^2_{M-S_2}}=22.9\%$ of when considering OCS in the fit, and a reduction of the χ_ν^2 by $1-\frac{\chi^2_{M-S_1}}{\chi^2_{M-S_3}}=8.9\%$ when setting to zero the OCS signature in the synthetic spectrum S_3 compared to S_1. The definition of the different spectra is the same as in section 3.4.1.

We also computed the histogram of the distribution of the weighted residuals, see the right panels of Fig. 3, and we see a 4σ significative decrease of the σ_H-value of the Gaussians when considering OCS in the fit.

The fitted OCS integrated slant density is equal to $4.48\times10^{17}\pm1.26\times10^{17}$ cm^{-2}, and the upper-limit detection is equal to 2.78×10^{13} cm^{-2}, with a local number density at 81.6 km equal to $1.16\times10^{10}\pm8.04\times10^{8}$ cm^{-3}.

3.4.3. *Sulfur trioxide*

The SO_3 fit is illustrated with occultation 488.2, taken on 22 August 2007 at a latitude of 37°N and a longitude of 253°W, on the morning side of the terminator.

SO_3 was positively detected in the spectrum taken in order 125 bin #2 at a tangent altitude of 74.2 km, and the corresponding best fit of the slant density is given in Fig. 4. All criteria are satisfied: including SO_3 in the fit reduces χ_ν^2 by $1-\frac{\chi^2_{M-S_1}}{\chi^2_{M-S_2}}=13.1\%$ and comparing S_1 with S_3 where the SO_3 signature is set to zero reduces the χ_ν^2 by $1-\frac{\chi^2_{M-S_1}}{\chi^2_{M-S_3}}=43\%$. The correlation between measured and synthetic spectra increases by $1-\frac{corr_{(M,S_2)}}{corr_{(M,S_1)}}=0.27\%$, and by $1-\frac{corr_{(M,S_3)}}{corr_{(M,S_1)}}=0.1\%$.

The fit of a Gaussian on the histogram of the distributions of the weighted residuals provided in the right panels of Fig. 4 also shows a 1σ significative reduction of the χ_ν^2.

The fitted SO_3 integrated slant density is equal to $3.09\times10^{19}\pm6.6\times10^{18}$ cm^{-2}, and the upper-limit detection is equal to 2.11×10^{15} cm^{-2}, with a local number density at 74.2 km equal to $2.48\times10^{11}\pm6.86\times10^{10}$ cm^{-3}.

3.4.4. *Carbon monosulfide*

We present the fit of CS in order 111, relative to the detection during orbit 3052.1 in bin #2 at an altitude of 72.5 km, on 25 August 2014 at a latitude of 87°N, a longitude of 181°W, on the morning side of the terminator, see Fig. 5.

In this order, CO_2, SO_2, and CS absorb. The SO_2 detection is discussed in section 3.4.1, and SO_2 was not positively detected in this particular spectrum. There is a reduction in χ_ν^2 when comparing S_1 and S_2 by $1-\frac{\chi^2_{M-S_1}}{\chi^2_{M-S_2}}=7\%$ while considering CS in the fit of the spectrum, and a decrease in χ_ν^2 when comparing S_1 and S_3 by $1-\frac{\chi^2_{M-S_1}}{\chi^2_{M-S_2}}=5.8\%$ while setting the CS signature to zero in the fit of the major and minor species. There is an increase of the correlation when comparing S_1 and S_2 to M by $1-\frac{corr_{(M,S_2)}}{corr_{(M,S_1)}}=0.04\%$, and by $1-\frac{corr_{(M,S_2)}}{corr_{(M,S_1)}}=0.08\%$ when comparing S_1 and S_3 to M.

The histograms of the distributions of the weighted residuals, and the corresponding Gaussian fits, see the right panels of Fig. 5, show that

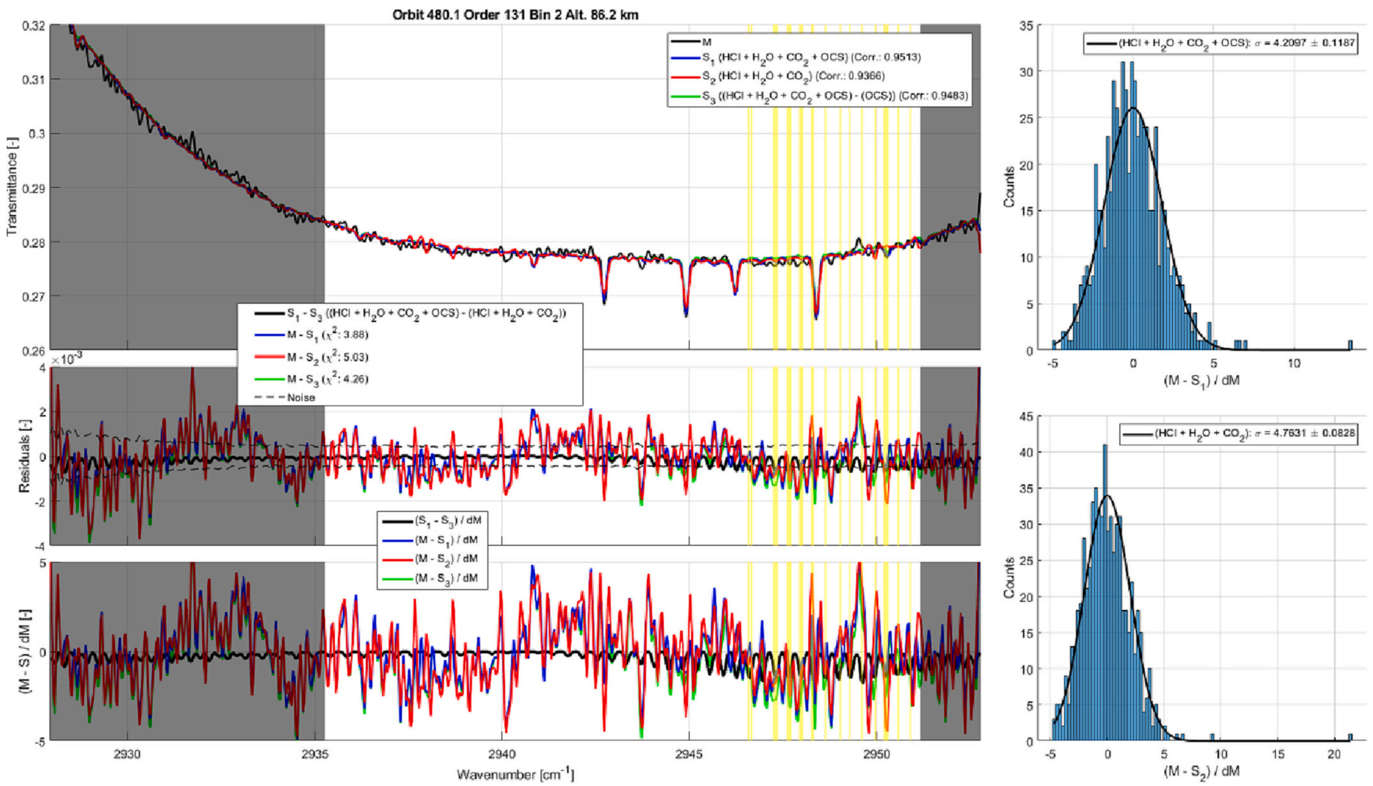

Fig. 3. Same as Fig. 2 for an example of OCS fit.

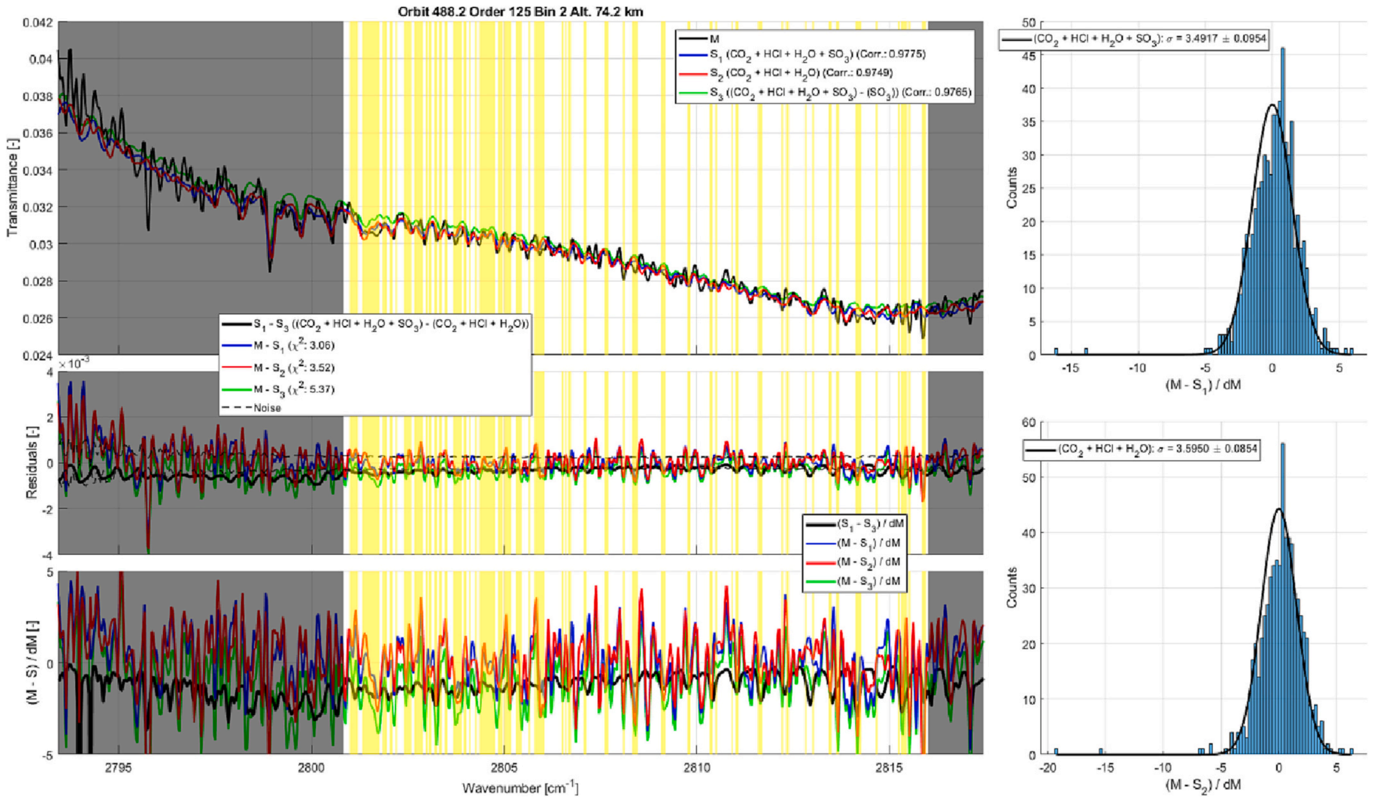

Fig. 4. Same as Fig. 2 for an example of SO_3 fit.

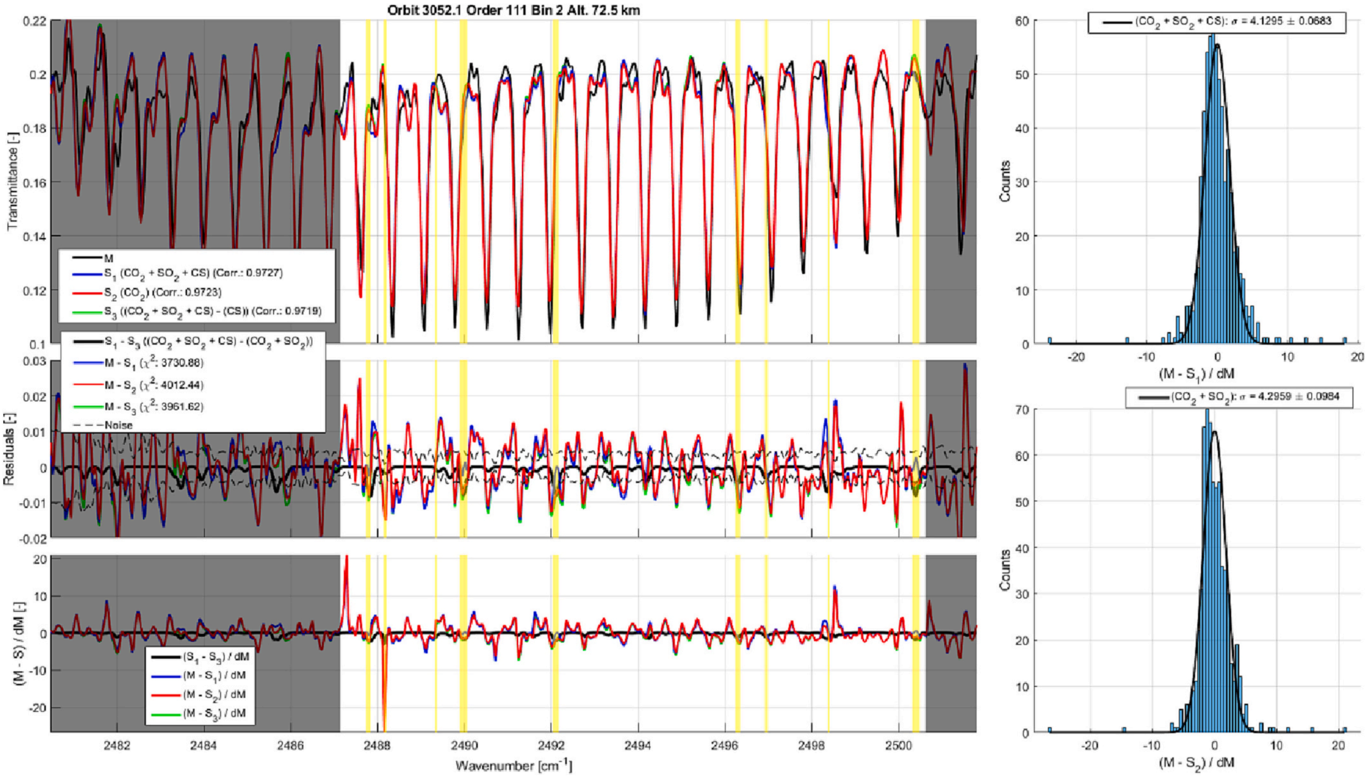

Fig. 5. Same as Fig. 2 for an example of CS fit.

when considering the σ_H-values of the Gaussian fits, we have a 1σ significative reduction of the χ_ν^2 when considering S_1 rather than S_2.

The retrieved CS integrated slant density is equal to 3.87 × 10^{18} ± 7.69 × 10^{17} cm^{-2}, and the upper-limit detection is equal to 5.44 × 10^{13} cm^{-2}, with a corresponding local number density of 3.53 × 10^{11} ± 7.01 × 10^{10} cm^{-3}.

3.4.5. Carbon disulfide

CS_2 was detected in order 126 during orbit 1044.1 in bin #2 at an altitude of 78.5 km, on 28 February 2009 at a latitude of 77°N, a longitude of 155°W, on the morning side of the terminator, see Fig. 6. In order 126, CO_2, HCl, H_2O, SO_3, and CS_2 absorb. The SO_3 detection is discussed in section 3.4.3 while it was not positively detected in the spectrum presented here.

There is a reduction in χ_ν^2 by $1-\frac{\chi^2_{M-S_1}}{\chi^2_{M-S_2}} = 5.9\%$ while considering CS_2 in the fit of the spectrum, and a reduction of χ_ν^2 by $1-\frac{\chi^2_{M-S_1}}{\chi^2_{M-S_3}} = 9\%$ when comparing S_1 and S_3, i.e. the spectrum of the best fit while considering major and minor species (S_1) compared to the same best fit but setting the CS_2 signature to zero (S_3). There is an increase of the correlation by $1-\frac{corr_{(M,S_2)}}{corr_{(M,S_1)}} = 1.1\%$ between the measured and fitted spectra while considering CS_2 in the fit, and an increase of the correlation when considering S_1 and S_3 by $1-\frac{corr_{(M,S_3)}}{corr_{(M,S_1)}} = 0.9\%$.

The histogram of the weighted residuals of the measured spectrum M with S_1, the fit of the major and minor species, and the histogram of the weighted residuals of M with S_2, the fit of the major and non-targerted minor species S_3, are also provided in the right panels of Fig. 6. The σ_H-value of the fits of the Gaussians on the histograms shows that we have a nearly 2σ significative difference between the distributions.

The retrieved CS_2 integrated slant density is equal to $2.44 \times 10^{18} \pm 6.41 \times 10^{17}$ cm^{-2}, and the upper-limit detection is equal to 1.19×10^{17} cm^{-2}, with a corresponding local number density of $3.25 \times 10^{10} \pm 1.35 \times 10^{10}$ cm^{-3}.

3.5. Fitted calibration parameters

Three calibration parameters are fitted together with the species number densities and the baseline parameters: variations to the instrument resolution (1 variable), variation to the wavenumber position of the AOTF transfer function (1 variable), and variations to the pixel to wavenumber calibration (5 variables), the latest given as a fourth-order polynomial. The temperature proxy is also fitted and is discussed separately in section 3.6. As explained above, these parameters are fitted to enhance the quality of the fit, because they might vary during an observation due to temperature changes within the SOIR instrument.

In Fig. 7, we show how these parameters vary for the fit of the transmittances measured during orbit 341.1 while targeting SO_2, which recorded order 112 where SO_2 and CS absorb. There are two transmittance datasets, corresponding to bins #1 and #2. For all parameters, very similar values are obtained for the S_1 (fit of the major and minor constituents) and S_2 fits (fit of major constituents only and non targeted minor species). The fitted instrument resolution (left panel) always lies within the uncertainty of this instrument variable (Mahieux et al., 2008). The center of the AOTF transfer function (center panel) slightly varies during the occultation, most probably due to temperature variations within the instrument (Mahieux et al., 2009). Finally, very small wavenumber shifts are observed when fitting an improvement to the pixel-to-wavenumber calibration. We note that the pixel to wavenumber calibration already includes the Doppler shifts due to the spacecraft motion relative to Venus (Mahieux et al., 2008).

3.6. Impact of the temperature proxy on the retrieval

First, we note that since we use the temperature profile retrieved from the CO_2 number densities measured by SOIR and the hydrostatic equilibrium (Mahieux et al., 2015a), the temperature adjustment in the spectral fits is negligible.

We study how the retrievals are impacted by the temperature profile, by building three sets of synthetic spectra with three different temperature profiles. Fits of these spectra are achieved and compared to each other.

We consider an SO_2 retrieval of synthetic spectra built considering the same procedure as the one described in section 3.3, i.e. building

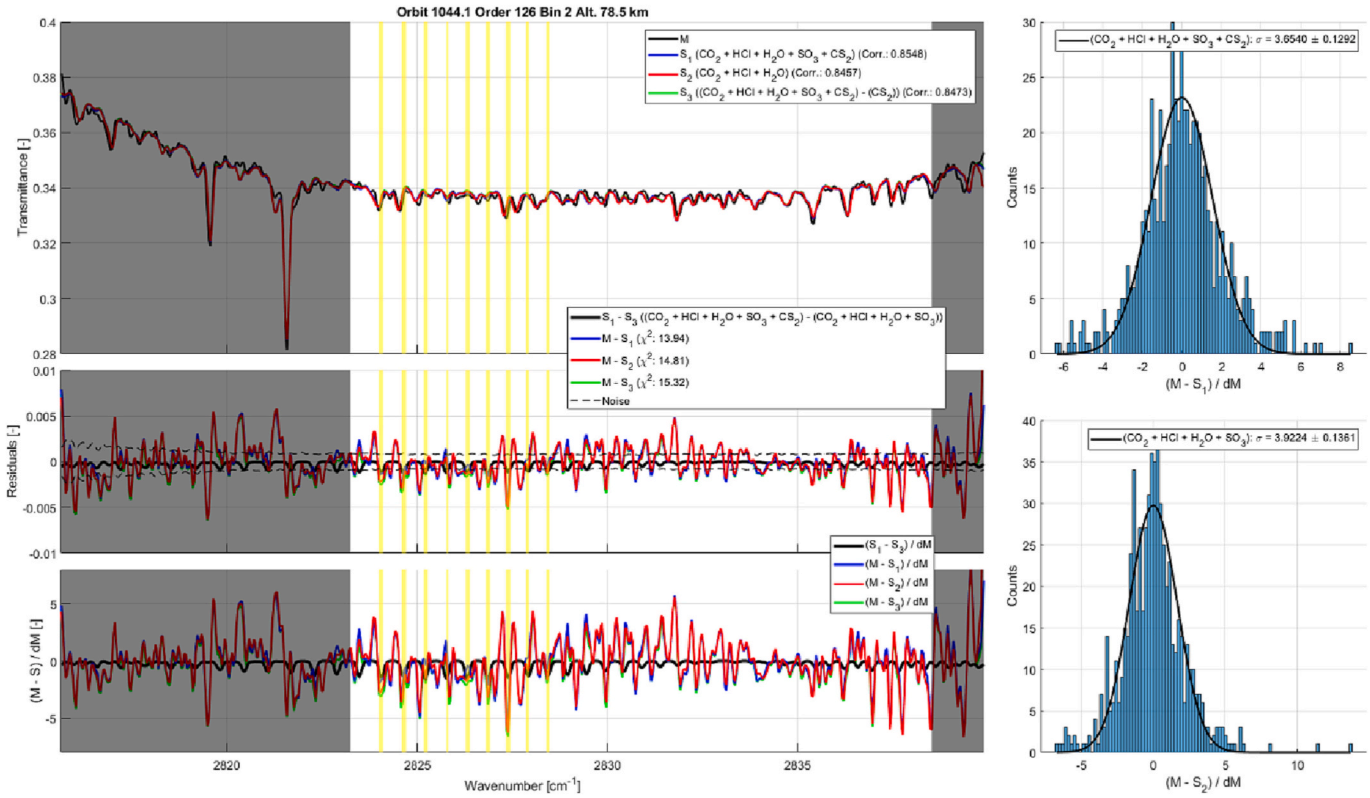

Fig. 6. Same as Fig. 2 for an example of CS_2 fit.

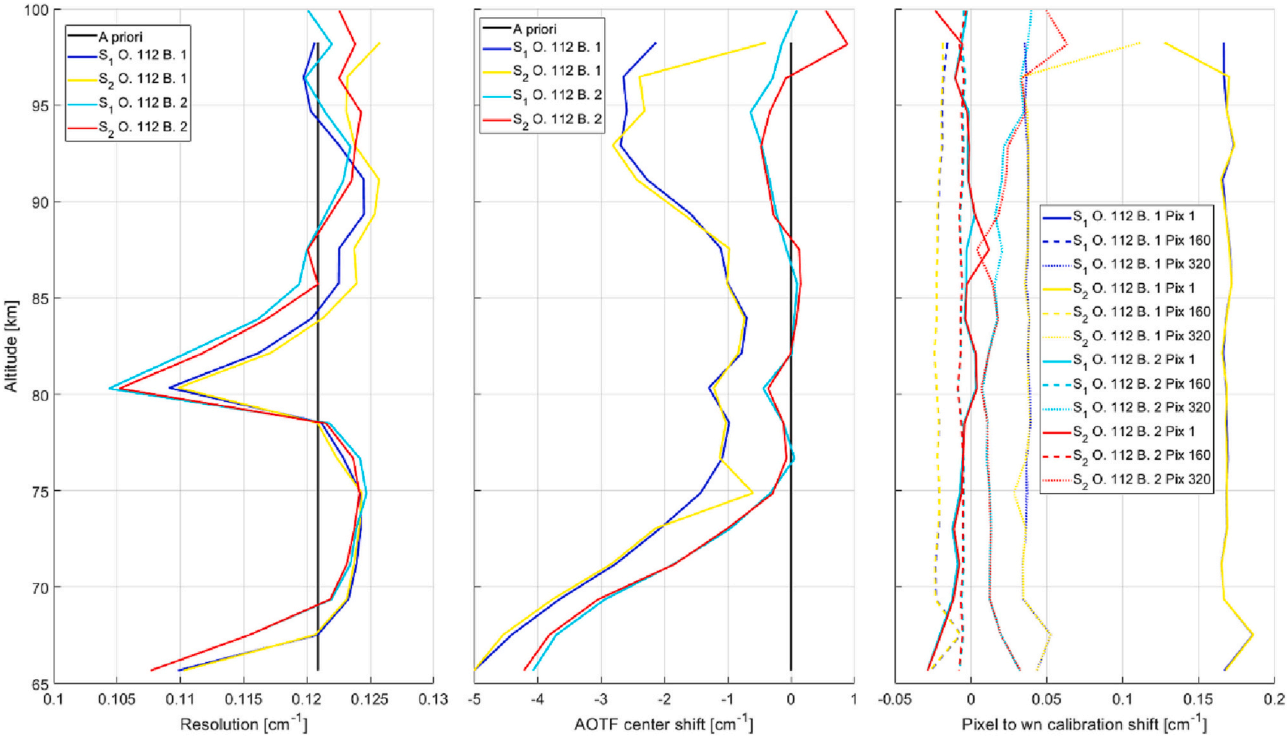

Fig. 7. Example of retrieval of instrument parameters for orbit 341.1 in order 112 for bins 1 and 2 for fits S_1 and S_2. In the legends, “O.” stands for order and “B.” for bin. (Left panel) Fit of the instrumental resolution. (Center panel) Fit of the displacement of the maximum of the AOTF transfer function. (Right panel) Wavenumber displacement of pixels 1, 160, and 320 after adjusting the pixel to wavenumber calibration.

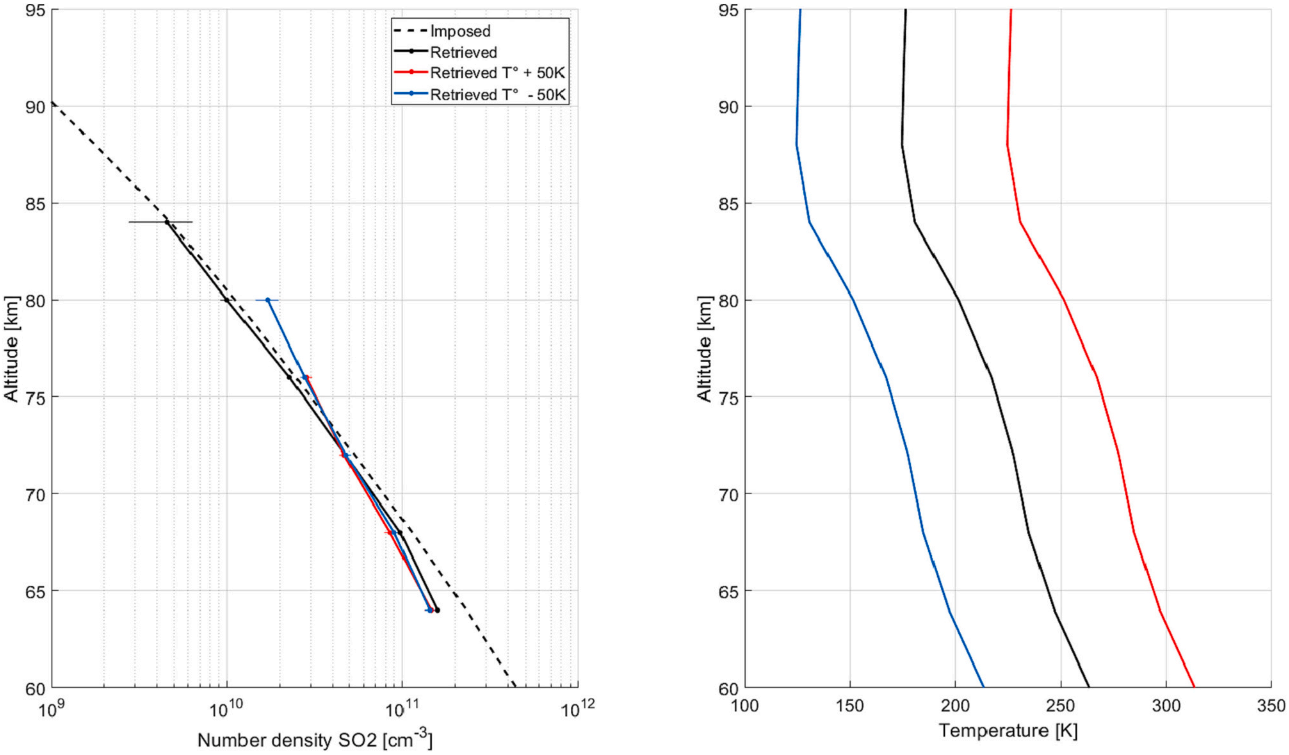

Fig. 8. Comparison of the retrieval of synthetic SO_2 spectra in orders 110, 111, and 112 using three different temperature profiles: VIRA (in black), VIRA +50 K (in red), and VIRA – 50 K (in blue). The left panel shows the retrieved profiles (plain curves) with the uncertainties and the profile used to build the spectra (named “Imposed”). The right panel shows the three temperature profiles used to build the spectra. (For interpretation of the references to color in this figure legend, the reader is referred to the web version of this article.)

synthetic spectra considering known CO_2, CS, and SO_2 vertical profiles corresponding to a SO_2 VMR of 70 ppb (constant with altitude), CS VMR of 10 ppb, and CO_2 at 96.5%, and adding noise equivalent to a SNR of 2000, typical for SOIR. However, instead of focusing on a single altitude as presented in section 3.3, we consider the altitude range from 85 km down to 60 km. We build three sets of spectra, for each of the orders in which SO_2 absorb, i.e. 110, 111, and 112. We consider three cases; in the first one, we use the temperature profile from VIRA; in the second one, we add 50 K to the VIRA profile at all altitudes; finally, in the third one, we subtract 50 K from the VIRA profile. We use the criteria defined in section 3.2, and we merge the positive detections obtained in each order 110, 111, and 112. The results are given in Fig. 8, where we show the retrieved SO_2 number densities in the left panel based on the temperature profiles used to build the synthetic spectra in the right panel. We see that the retrieved profiles are slightly dependent on the temperature profile used to build the spectra, and are overall in good agreement with the SO_2 number density profile used to build the synthetic spectra.

4. Results

4.1. Sulfur dioxide

Two hundred forty-five SO_2 detections were attempted, 155 successful detections were obtained (63.3% detection rate in terms of orbits). SO_2 was detected at all latitudes; we do not report any latitude or side of the terminator dependence of the measured VMRs.

The SO_2 VMRs are presented in Fig. 9; they are computed considering total densities from VIRA (Keating et al., 1985; Zasova et al., 2006). The uncertainties are not plotted for clarity, and they vary between 10 and 100% of the retrieved value. The color code indicates the reduction of χ_ν^2 that is obtained while adding SO_2 to the spectral fit (criteria *a*), and the filled and empty markers indicate if the local number density exceeds the detection limit or the white noise limit, respectively (criteria *b*).

SOIR also reported CO_2 and temperature profiles (Mahieux et al., 2015a), from which a total density can be computed while assuming the CO_2 VMR from VIRA (Keating et al., 1985; Zasova et al., 2006). We decided to provide the minor species VMR considering the total density from VIRA (1) in order to be consistent with previous studies, since the CO_2 VMR from SOIR is often half-an-order to an order of magnitude lower than the VIRA values; (2) to obtain a consistent database since SOIR did not always measure CO_2 during an occultation or in the same altitude region as SO_2 was measured, and (3) because we use the CO_2 VMR from VIRA to compute the total density, which does not make the total densities totally independent from VIRA.

The general tendency shows constant VMRs between the cloud top and 90 km of altitude, followed by an increase in VMR with altitude. The SO_2 number densities and VMRs are highly variable; the VMRs span nearly five orders of magnitude. Such a large variability was also reported for upper cloud measurements by Encrenaz et al. (2012) and Encrenaz et al. (2016) using TEXES. We compare the SO_2 VMR to several literature values in Fig. 9. We compare with the mean nightside profile obtained by the SPICAV-UV/VEx instrument on board VEx (Evdokimova et al., 2021), which detected SO_2 at higher altitudes and also reported a large variability. The SPICAV-UV/VEx mean profile covers the same time period as the profiles discussed in this work and is in good agreement. Two exemplary profiles measured in the microwave by Sandor et al. (2010) are also plotted; they show a sharp discontinuity in the SO_2 VMR at an altitude of ~85 km such that the value below that altitude drops rapidly to a constant value of 10 ppb while remaining roughly constant at ~75 ppb at all altitudes above 85 km. The Sandor et al. (2010) retrievals and the mean profiles of this work are in reasonable agreement below 75 km (when the retrieval uncertainty is included) and

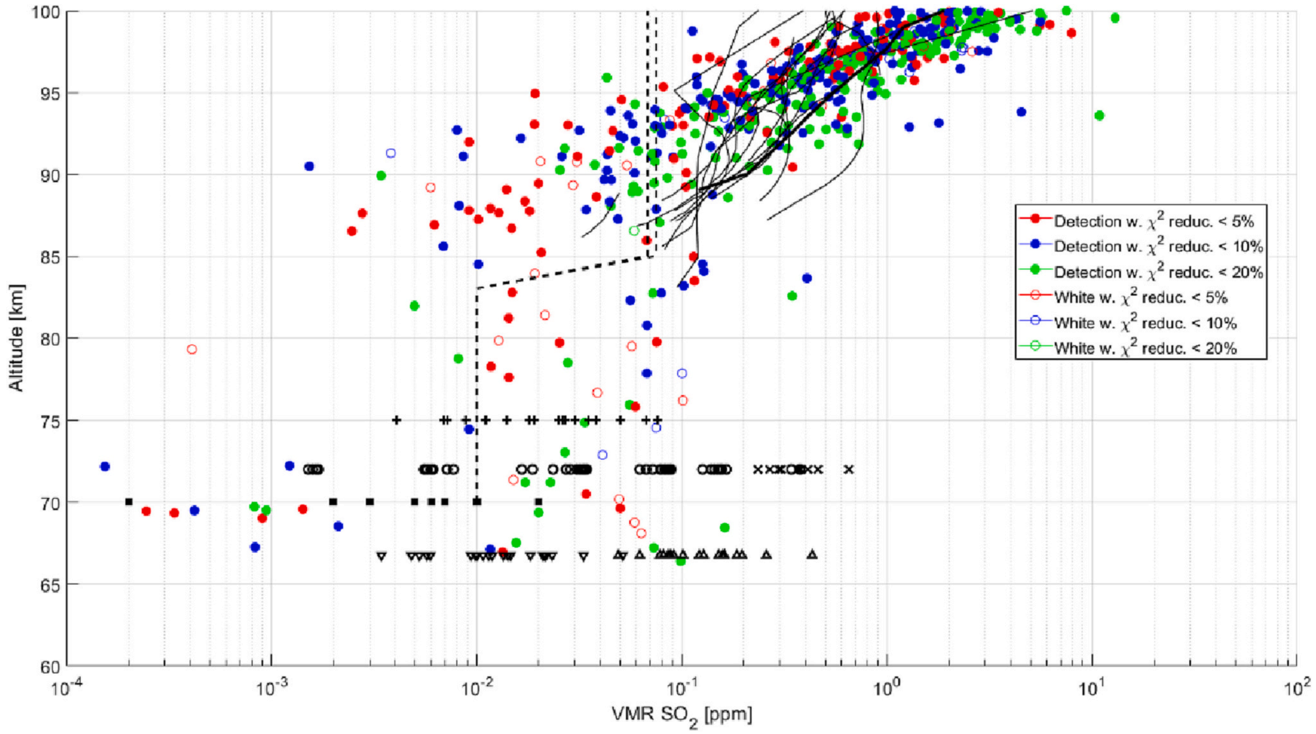

Fig. 9. SO_2 VMR considering the total number density from VIRA (the reader is referred to the implications it has on the results that are described in section 3.1). The uncertainties are not displayed for clarity. The color code indicates the reduction of χ_ν^2 that is obtained while adding SO_2 to the spectral fit (criterion a), and the filled and empty markers indicate if the local number density exceeds the detection upper limit or the white noise upper limit, respectively (criterion b). The black symbols correspond to literature values: ▼ for Esposito et al. (1988), ▲ for Esposito et al. (1997), ○ for Marcq et al. (2011), ■ is the mean value from Marcq et al. (2020), × for Krasnopolsky (2010), + and the black dashed lines for Sandor et al. (2010), the thin black solid lines correspond to individual retrievals from Belyaev et al. (2017), and the red thick plain line is the mean profile from Evdokimova et al. (2021). (For interpretation of the references to color in this figure legend, the reader is referred to the web version of this article.)

the median of the SO_2 VMR values retrieved by SOIR overlap with the Sandor et al. results between 88 and 94 km. Although the SOIR retrieved SO_2 densities are relatively constant in the altitude range from 84 to 100 km, the corresponding SO_2 VMR inferred using the VIRA total density shows an increase in value with altitude at ~93–94 km and higher – a result not inferred from the Sandor et al. (2010) observations. Independent of the nuances in the ALMA, JCMT, and SOIR data retrieval comparisons, comparison of the SOIR values with the near and above cloud top SO_2 gas retrievals derived from Esposito et al. (1988), Esposito et al. (1997), Krasnopolsky (2010), Marcq et al. (2020), and Marcq et al. (2011) show strong agreement in value and temporal variability.

Mahieux et al. (2015b) derived SO_2 profiles from the same dataset and detected SO_2 in more observations than in the current work. Moreover, they obtained larger number densities and VMRs than the ones reported here. We explain these differences from various improvements made to the retrieval code ASIMAT: (i) the pixel-to-wavenumber calibration was substantially improved in this work, (ii) more robust and strict criteria for the minor species detections are implemented in the revised version of ASIMAT, as explained in section 3.

The detections at higher altitude have larger VMRs than the ones at low altitude, and this could be an artefact from the measurement technique we use: the upper limit profiles have larger values at high altitude, decreasing at lower altitude, see for example Fig. 19 with the upper limit profiles of H_2S and HOCl in section 4.6. Thus, low VMRs at high altitude could not be detected by the instrument, which can reconcile our results with Sandor et al. (2010). For this reason, we do not present mean profiles in this work, neither for SO_2 nor for the other species.

Finally, we computed histograms of the SO_2 detection as a function of time, latitude (assuming Equatorial symmetry), and local solar time (LST), see Fig. 10. The histogram represents the number of times SO_2 was detected in a spectrum, relative to the total number of spectra (not to the total number of orbits). The numbers presented here are different from the ones reported at the beginning of this subsection, as the detections per orbits were considered there, and not in terms of spectra as discussed here. We note that these results might be biased by the detection limit of the SOIR instrument, which is mostly a function of the SNR in the spectra, which is function of the measured orders (see Table 1). We compute the 1-σ uncertainty on the detection percentage given in the lower panel by assuming a random normal distribution of the observations. For the time dependency, the bins were chosen to be linked to a Venus orbital characteristic and to cover enough SOIR observations. We observe a decrease of detection percentages during the time of the mission, from ~18% over the first two Venus years of the mission to ~8% at the end. This result can be linked to the SO_2 decrease at the Venus cloud top reported by Marcq et al. (2013), and confirmed in Marcq et al. (2020). Marcq et al. (2020) observed a latitude dependence of the SO_2 VMR at 70 km, with larger values at the Equator and decreasing towards the Poles, while the opposite behavior is observed for the SO_2 at the lower clouds (Oschlisniok et al., 2021). We observe the opposite dependency as a function of the absolute latitude (see center panels of Fig. 10). We note that Marcq et al. (2020) compared the concentrations, while here we only look at detections. Marcq et al. (2020) also reports on the local time dependency of the mean SO_2 values at 70 km, with similar values at 6 AM and 6 PM local time, similar to our results presented in the right panels of Fig. 10.

4.2. Carbonyl sulfide

One hundred fifty-seven occultations targeted orders in which OCS absorbs. OCS could be detected in at least one spectrum of 42 occultations (26.8%). The OCS detections cover all latitudes from pole to pole and span over the whole mission.

The positive detection OCS VMRs, presented in Fig. 11, respectively, show a variability spanning up to four orders of magnitude. The uncertainties are provided in the plot. The VMRs are computed considering

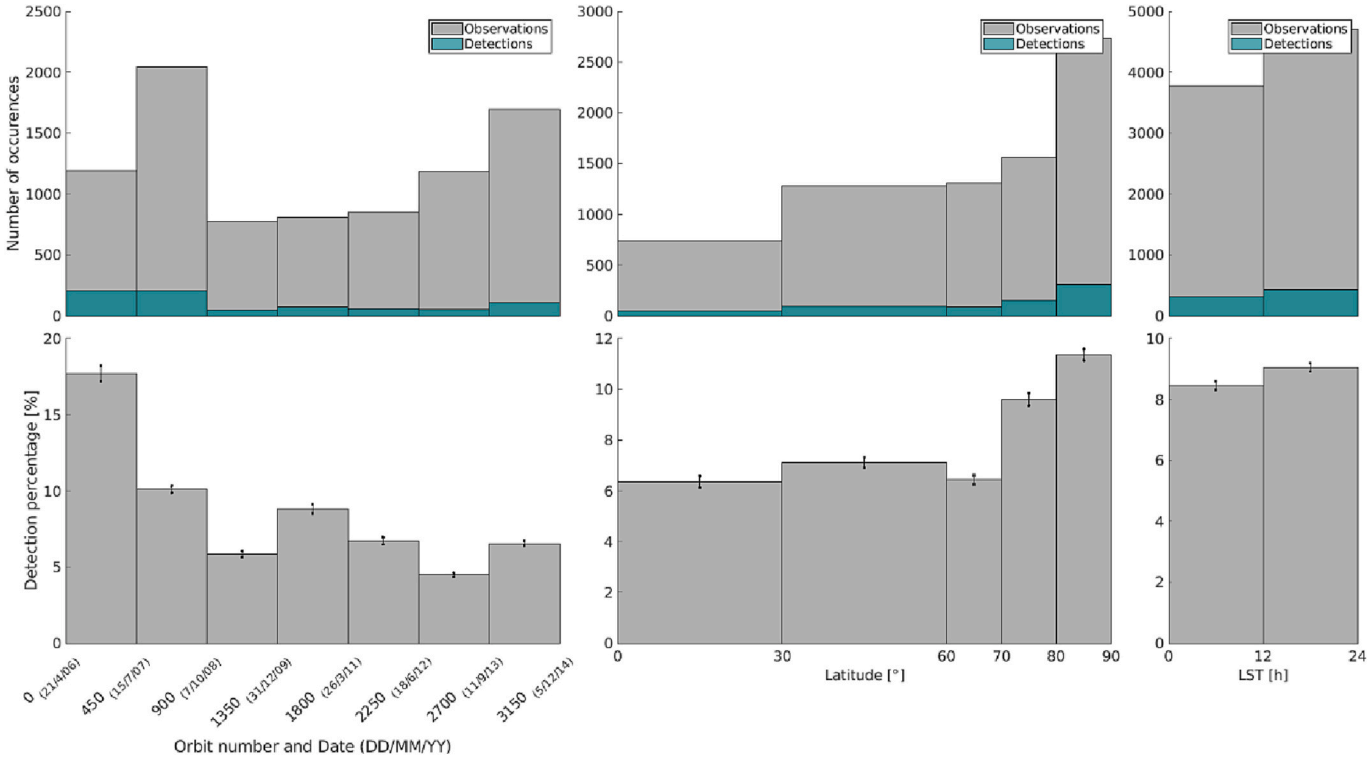

Fig. 10. Histograms of the detection rates per spectrum where SO_2 could be retrieved, see Table 1 for the list of orders. (Top panels) Histogram of the SO_2 observations and detections as a function of time using bins of 450 orbits (450 Earth-days or 2 Venus years) (top left panel), latitude (top center panel), and local solar time (top right panel). (Bottom panels) Histogram of the detection percentage as a function of time (bottom left panel), latitude (bottom center panel, assuming Equatorial symmetry), and local solar time (bottom right panel). The histogram is computed based on detections by individual spectra, rather than orbits.

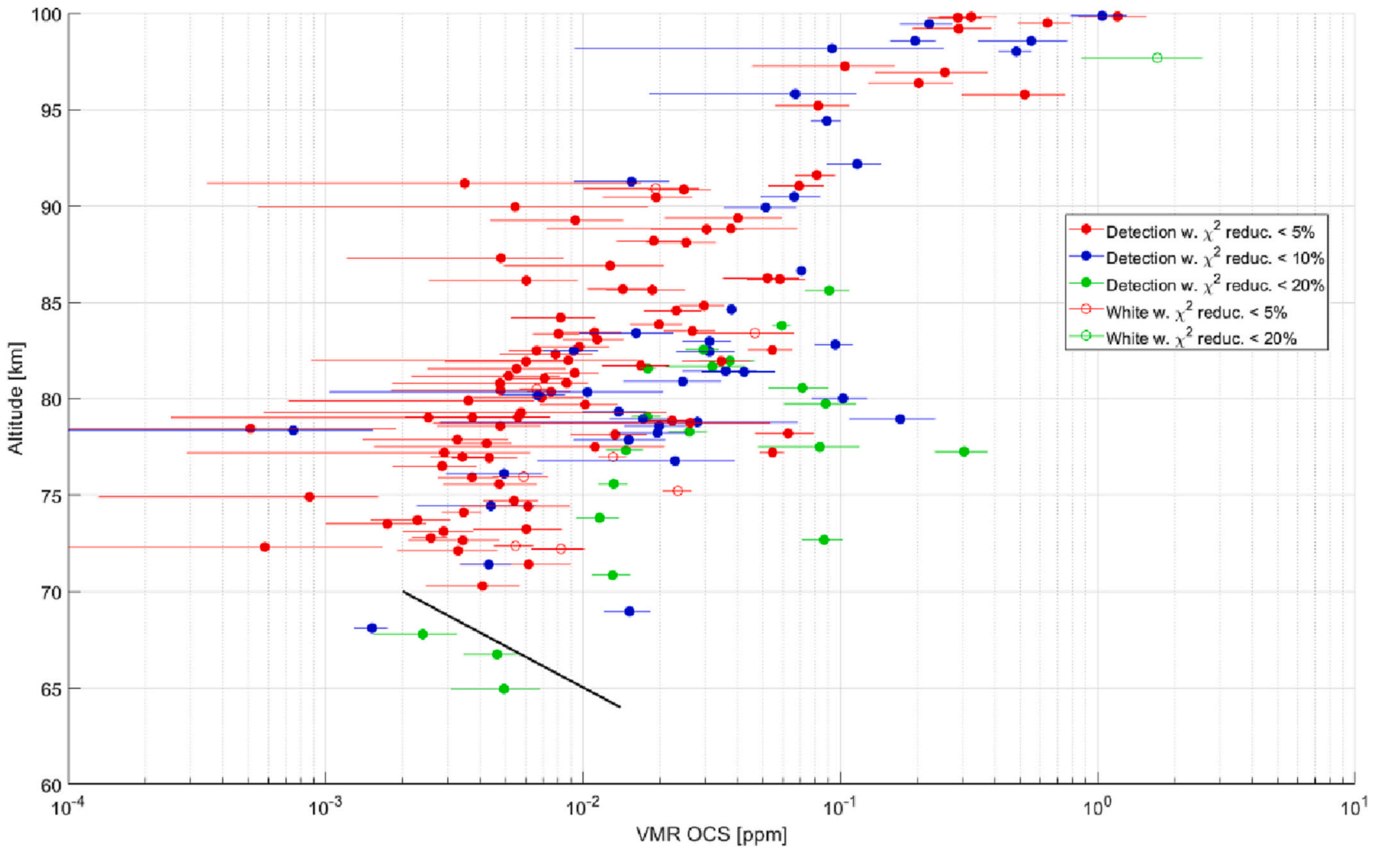

Fig. 11. OCS VMR considering the total number density from VIRA (the reader is referred to the implications it has on the results that are described in section 3.1). The uncertainties are the horizontal bars. The color code indicates the reduction of χ_ν^2 that is obtained while adding OCS to the spectral fit (criterion a), and the filled and empty markers indicate if the local number density exceeds the detection upper limit or the white noise upper limit, respectively (criterion b). The black line corresponds to value reported in Krasnopolsky (2010).

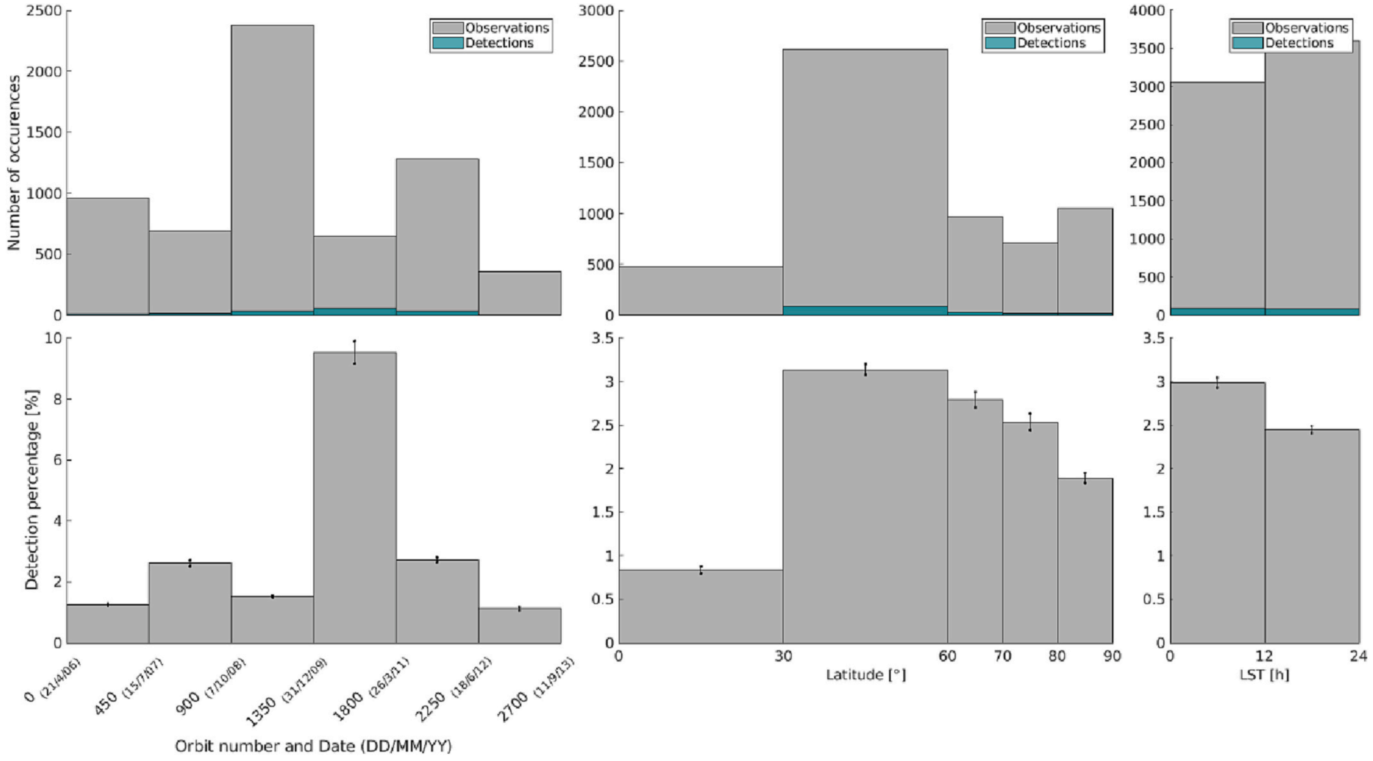

Fig. 12. Same as Fig. 10 for OCS detections.

the VIRA total densities. A mean profile might be biased to higher VMRs because of the lesser capacity of SOIR to detect low VMRs at higher altitude, for that reason we do not present mean profiles. The VMR has values around 3 ppb at 65 km increasing to 0.5 ppm at 100 km and shows a large variability up to a factor of 1000. We do not observe any latitude, time, or side of the terminator dependence of the OCS VMRs and number densities; the short-term and short-distance variability exceeds all other tendencies. The SOIR OCS detections are compared with the detection provided by Krasnopolsky (2010) below 70 km, and their values lie within the detections reported in this work. Other publications report on OCS values below the cloud top (Arney et al., 2014; Krasnopolsky and Pollack, 1994; Marcq et al., 2008; Marcq et al., 2005).

We looked at the long-term, latitude, and LST detection percentages in terms of spectra, provided in Fig. 12. As for SO_2, we note that these results might be biased by the detection sensitivity of the instrument, which is mostly a function of the SNR and the measured orders (see Table 1). We do not see any clear tendency of the OCS detection declining as a function of time as there is for SO_2, but rather a steady $\sim$2% rate of OCS detections during the whole VEx mission, except during years 8 to 10, where it increases to $\sim$9%, for no notable reason. This may have several implications. For example, the process depleting SO_2 with time may not apply to OCS or OCS population is retained at a constant level due to chemistry not linked to SO_2. There is some latitude dependency, with fewer detections ($\sim$1%) in the 0°-30° latitude region compared to the other latitude regions (2 to 3%). We do not see any significant dependency as a function of the side of the terminator.

4.3. *Sulfur trioxide*

Fifty-one occultations targeted orders in which SO_3 could be detected, and SO_3 was detected in at least one spectrum during 10 occultations (19.6%).

The VMR for each positive SO_3 detection is plotted in Fig. 13. The uncertainties are displayed as horizontal bars. All detections occurred between 70 and 100 km. This plot shows that among the retrieved SO_3 VMR values, the VMR values increase by a factor of 20 between 80 km and 95 km, from 0.5 to 10 ppm. However, repeated and long-term monitoring is needed to improve the statistical significance of the observed altitude variation. We note that, as for the other species, a mean profile might be biased to higher VMRs because of the lesser capacity of SOIR to detect low VMRs at higher altitude. We did not find any SO_3 detection above the cloud layer in the literature.

Zhang et al. (2012) and Bierson and Zhang (2020) simulated 1-D diurnally-averaged SO_3 profiles at 70° and 40° latitude, respectively, with both H_2SO_4 and H_2O fixed, so neither was a fully self-consistent calculation for the SO_2-H_2O-H_2SO_4 system. H_2SO_4 production is primarily limited by SO_3 production, which, in turn, is primarily limited by the upward flux of SO_2. Bierson and Zhang (2020) found SO_3 above the clouds has weak sensitivity to the chosen H_2SO_4 profile but strong sensitivity to the modeled SO_2 abundance at the cloud top and the presence/absence of a significant sulfur source above 95 km. Both modeling studies found SO_3 mixing ratios above $\sim$75 km are $\sim < 10$ ppb if modeled SO_2 is reasonably consistent with observed SO_2 and assumed H_2SO_4 is below the Sandor et al. (2012) upper limit. Thus, SO_3 in both models is a factor of 10–1000 smaller than our detections. Further work is needed to assess the compatibility between our SO_3 results and the H_2SO_4 upper limit from Sandor et al. (2012).

We look at the detection percentage in terms of spectra as a function of time, latitude, and local solar time in Fig. 14. As a function of time, we see a different pattern than the one of SO_2 in Fig. 10, with detections increasing between years 0–2 and 2–4, and decreasing in years 4–6. More detections are also observed in years 8–10, with levels similar to years 2–4. The fraction of detections in the mid-latitudes in the 30–60 latitude bins is double that in the equatorial and polar regions. There are

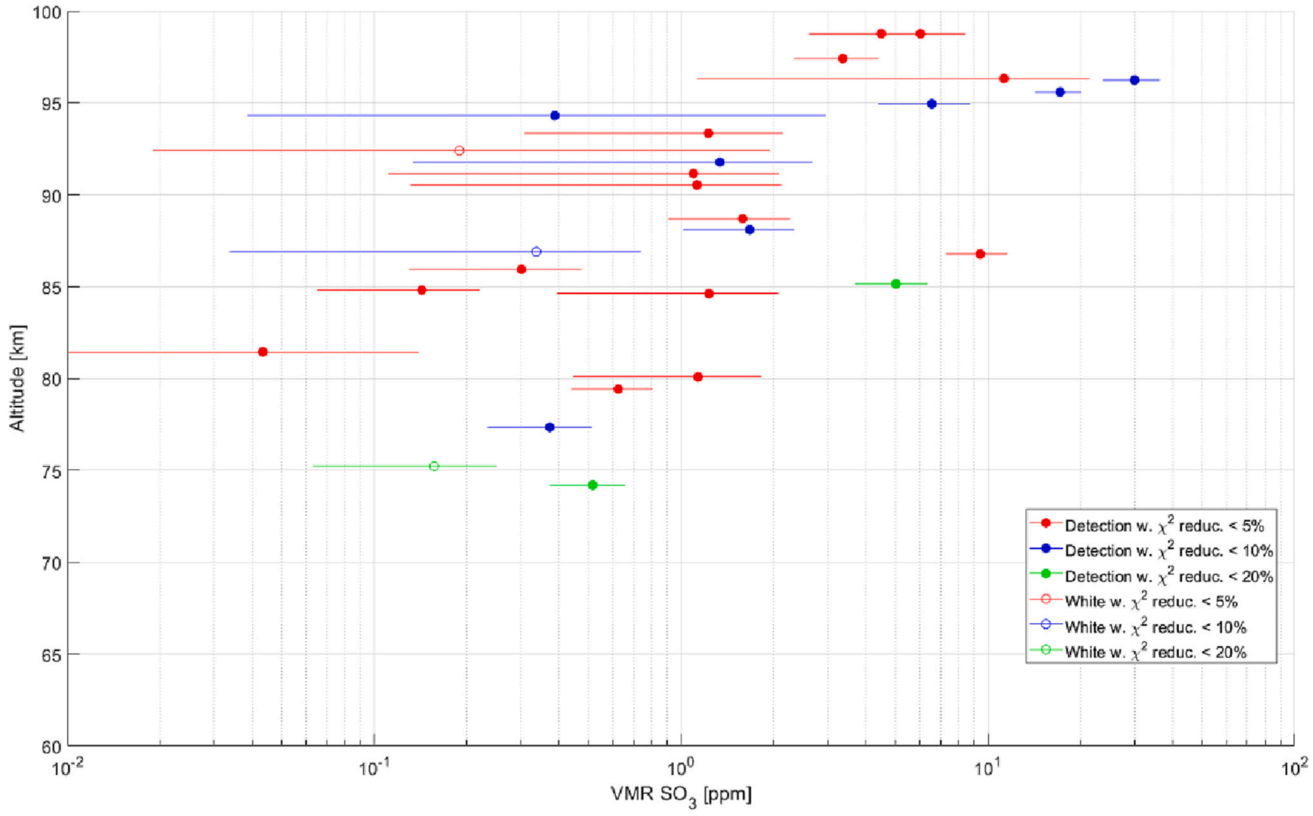

Fig. 13. SO_3 VMR considering the total number density from VIRA (the reader is referred to the implications it has on the results that are described in section 3.1). The uncertainties are the horizontal bars. The color code indicates the reduction of χ^2_ν that is obtained while adding SO_3 to the spectral fit (criterion a), and the filled and empty markers indicate if the local number density exceeds the detection upper limit or the white noise upper limit, respectively (criterion b).

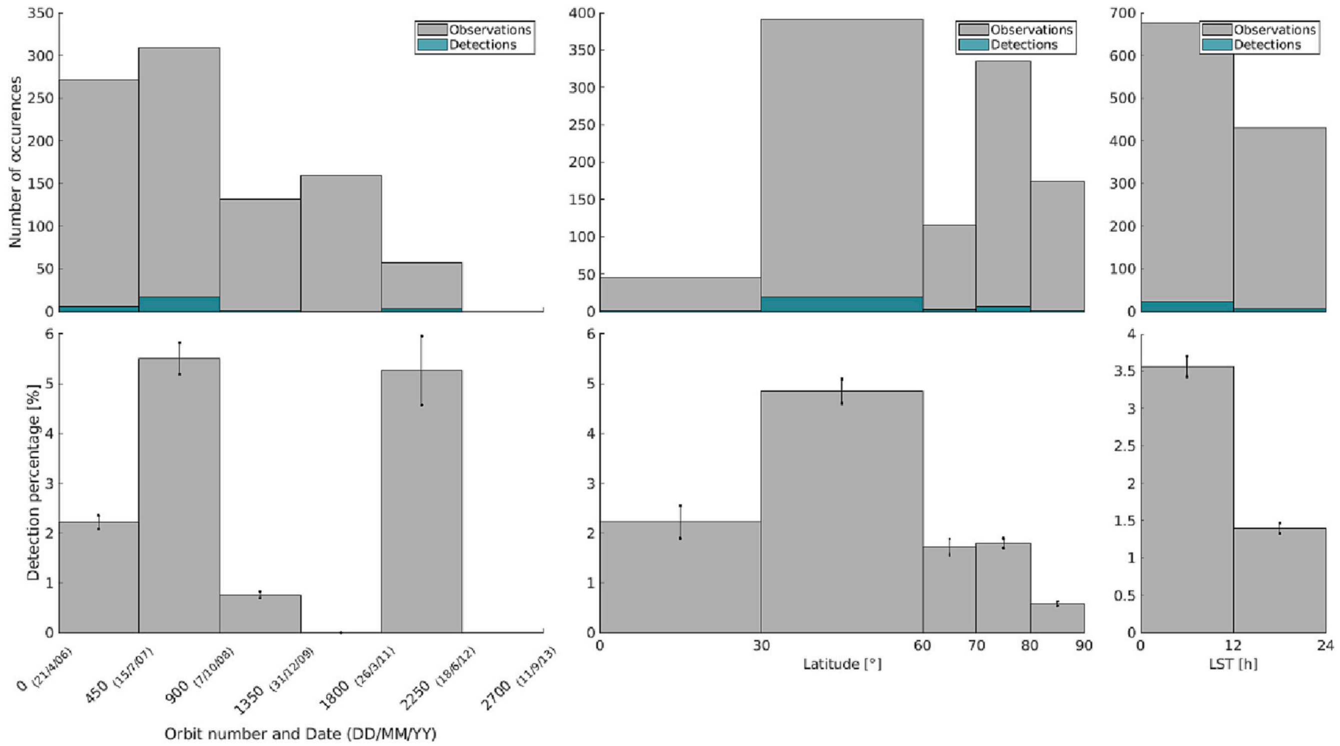

Fig. 14. Same as Fig. 10 for SO_3 detections.

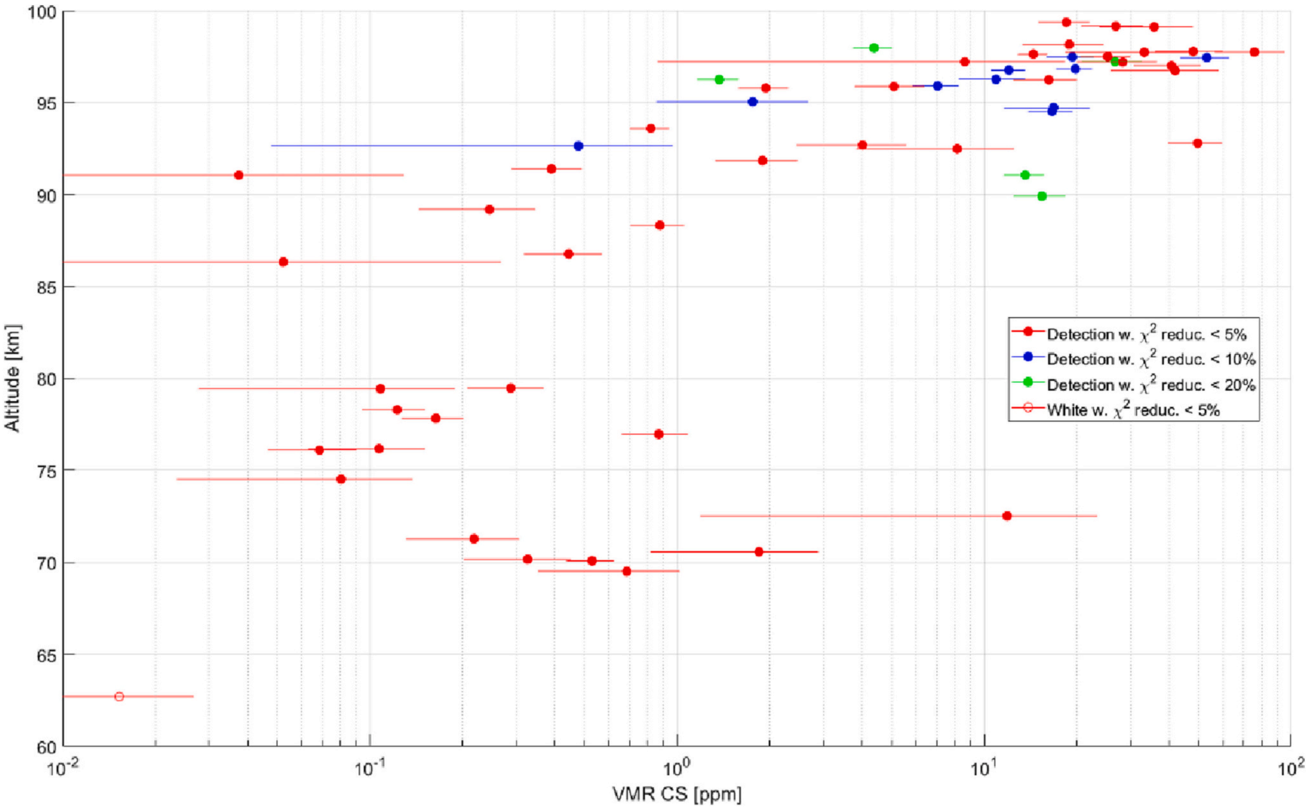

Fig. 15. CS VMR considering the total number density from VIRA (the reader is referred to the implications it has on the results that are described in section 3.1). The uncertainties are the horizontal bars. The color code indicates the reduction of χ_ν^2 that is obtained while adding CS to the spectral fit (criterion a), and the filled and empty markers indicate if the local number density exceeds the detection upper limit or the white noise upper limit, respectively (criterion b).

significantly more detections on the morning side of the terminator than on the evening side.

4.4. Carbon monosulfide

Two hundred forty-four occultations were targeting orders in which CS absorbs, covering all latitudes, both sides of the terminator, and the whole time of the VEx mission. CS could be detected in at least one spectrum of 30 occultations (12.3%).

Figure 15 presents the VMRs computed considering the VIRA total number densities together with the uncertainties. We observe an increase of the CS VMR at altitudes between 70 km and 100 km, from mean values of 0.1 ppm to 30 ppm. As for the other species, we note that the mean values at higher altitude might be biased to larger values due to the lack of sensitivity of the instrument at these altitudes, see section 3.3. We did not find any upper limit or detection values in the literature for CS.

Finally, we look in Fig. 16 at the detection distribution in terms of spectra as a function of time (left panel), latitude bins (center panel), and side of the terminator (right panel). These results might be biased by the SNR in the orders measured by SOIR. We observe an increase of the detections between Venus years 0–2 to 2–4 by 50% to nearly 8%, very few during Venus years 4–6 (~0.5%), followed by an increase in years 6–8 to levels equivalent to years 0–4 (~7%), finally followed by a decrease to values between 2 and 4%. We see a latitude dependence of the detections with values around ~2–3%, except in latitude bins 60°-70° and 70°-80°, where they increase to 6%. The low value in the 0–30° latitude bin needs to be considered carefully due to the low statistics in that latitude bin. Finally, there is no significant side of the terminator dependence, with values of ~3.5% detection. (See Fig. 16)

4.5. Carbon disulfide

CS_2 was targeted 25 times over the whole mission. Most of the measurements occurred in the Northern hemisphere, on both sides of the terminator, covering the whole mission duration. CS_2 could be detected in at least one spectrum of six SOIR occultations (24%).

The VMRs vary between 20 ppb at 75 km up to ~5 ppm at 95 km (See Fig. 17). As for the other species, a bias towards larger VMRs is observed at high altitude which may be due to the sensitivity of the instrument. CS_2 has not been included in recent photochemical models for Venus. Nevertheless, because CS is a direct photolysis product of CS_2, correlated detection of CS and CS_2 is expected. We point out that the detection of CS_2 is harder than detecting CS at IR wavelengths, because the CS_2 absorption cross-section is two times smaller than CS (see Fig. 1), i.e., one needs a larger SNR to positively detect CS_2 than to positively detect CS.

We also study the time, latitude, and LST dependency of the CS_2 detections in terms of spectra in Fig. 18. First, orders in which CS_2 absorbs were only merasured during the years 2 to 6. Over that time period, the detection levels are nearly constant around 2 to 2.5%. In terms of latitude dependence, the observations only occurred at latitudes larger than 70°, with equivalent levels. Finally, we see a large difference in terms of detections when comparing the two sides of the terminator, with detections only on the morning side, although observations were made on both terminators.

4.6. Upper limits on hypochlorous acid and hydrogen sulfide

HOCl was targeted only four times and could not be detected in the SOIR spectra. For this reason, we provide upper limit profiles; see the upper panels of Fig. 19. The upper limit values vary between 10^{-5} and 6 ppm at 60 km, and between 100 and 10^5 ppm at 100 km. The largest mixing ratio calculated for HOCl in the Zhang et al. (2012), Bierson and Zhang (2020), and Bains et al. (2021) models is $\sim < 10^{-5}$ ppm.

Three hundred thirteen occultations were targeting orders in which H_2S has strong enough spectral lines, and H_2S could not be firmly detected in any of those measurements. For this reason, we provide upper limit profiles in Fig. 19. The upper limit VMR values vary between 1 ppt and 100 ppm at 60 km, and 1 ppb and 0.01 at 100 km.

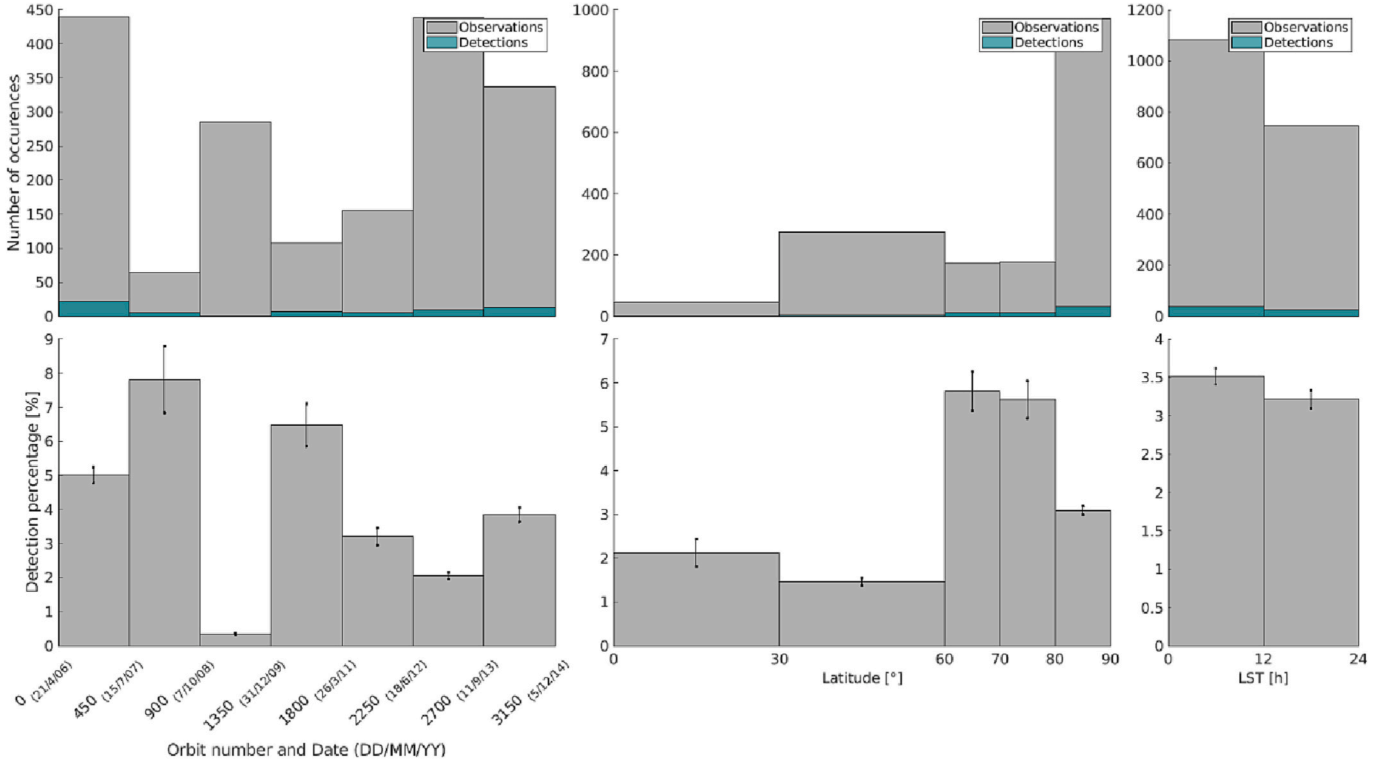

Fig. 16. Same as Fig. 10 for CS detections.

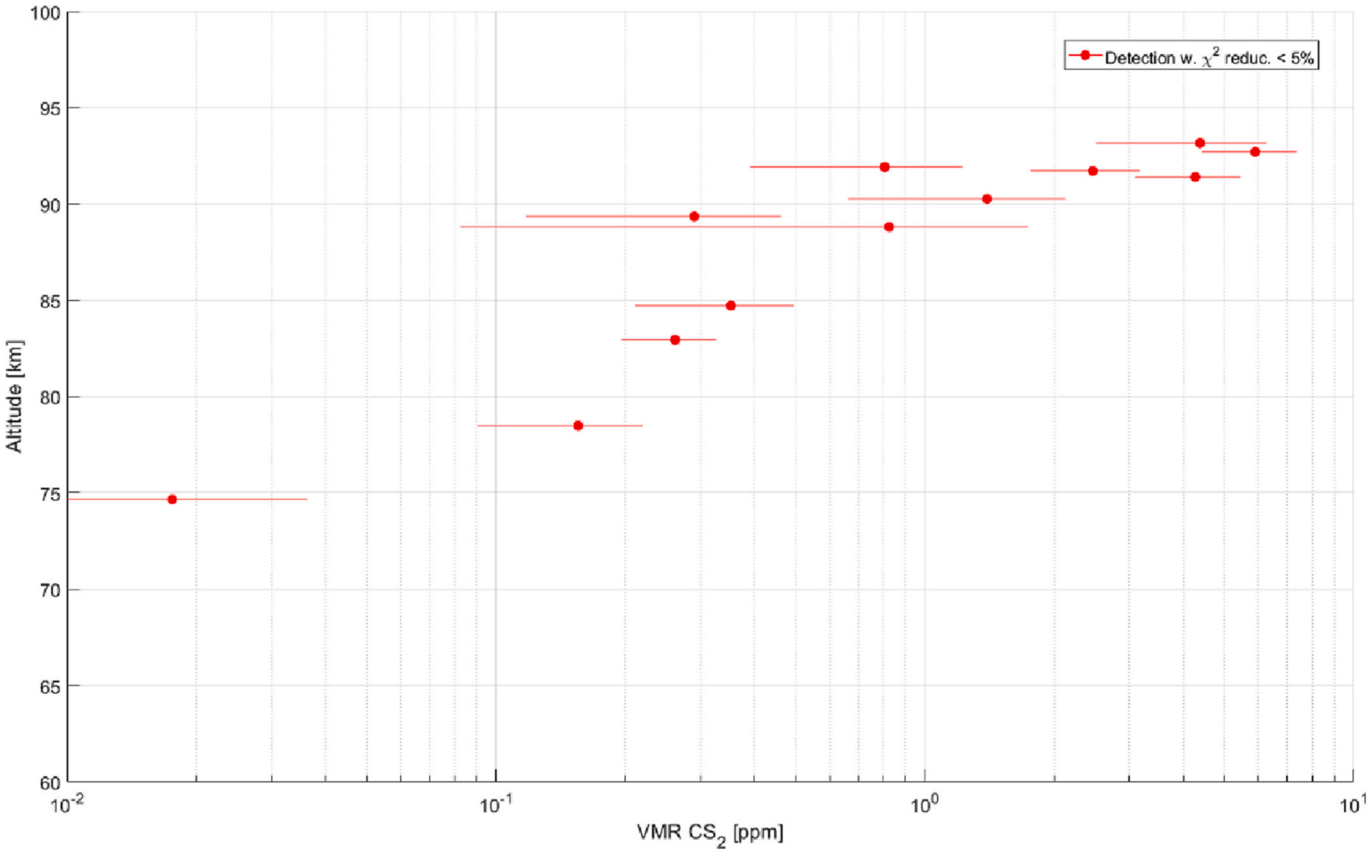

Fig. 17. CS_2 VMR considering the total number density from VIRA (the reader is referred to the implications it has on the results that are described in section 3.1). The uncertainties are not displayed for clarity. The color code indicates the reduction of χ^2_ν that is obtained while adding CS_2 to the spectral fit (criterion a), and the filled and empty markers indicate if the local number density exceeds the detection upper limit or the white noise upper limit, respectively (criterion b).

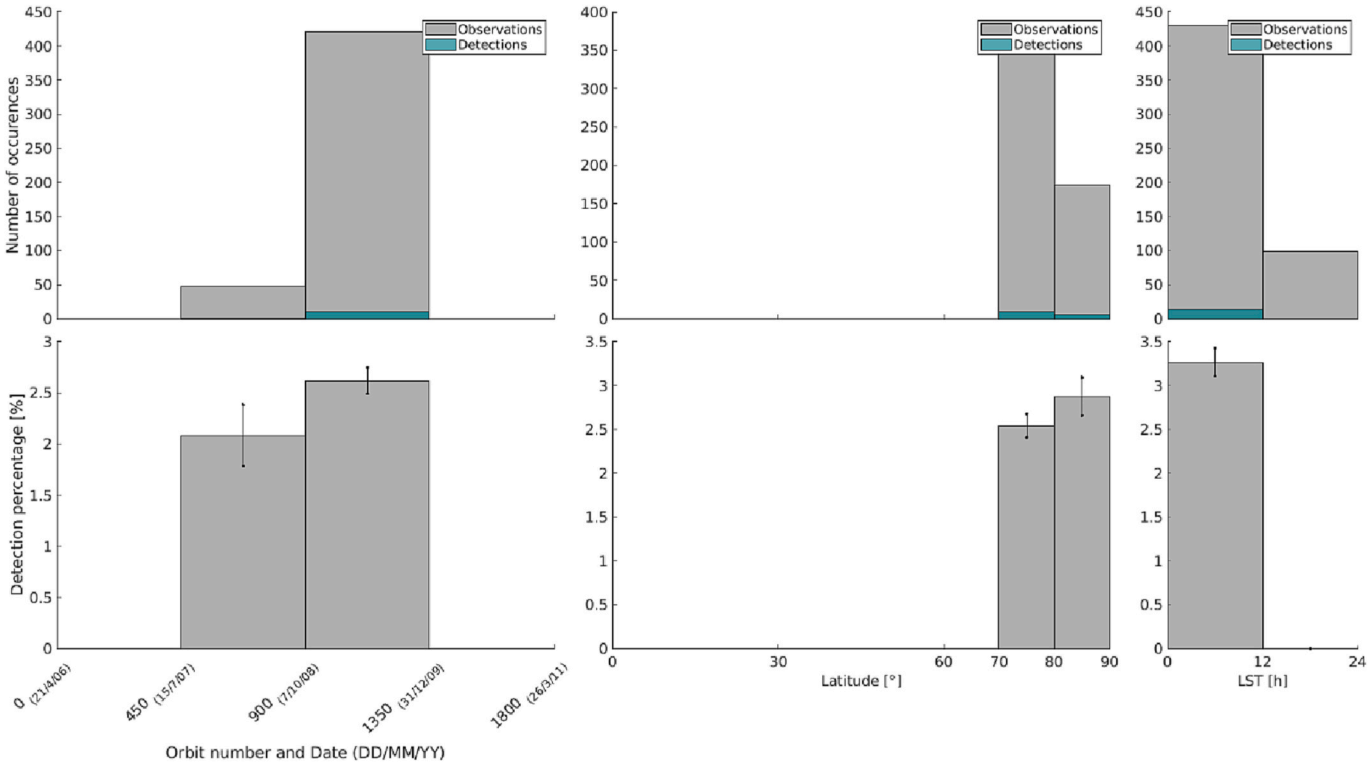

Fig. 18. Same as Fig. 10 for CS_2 detections.

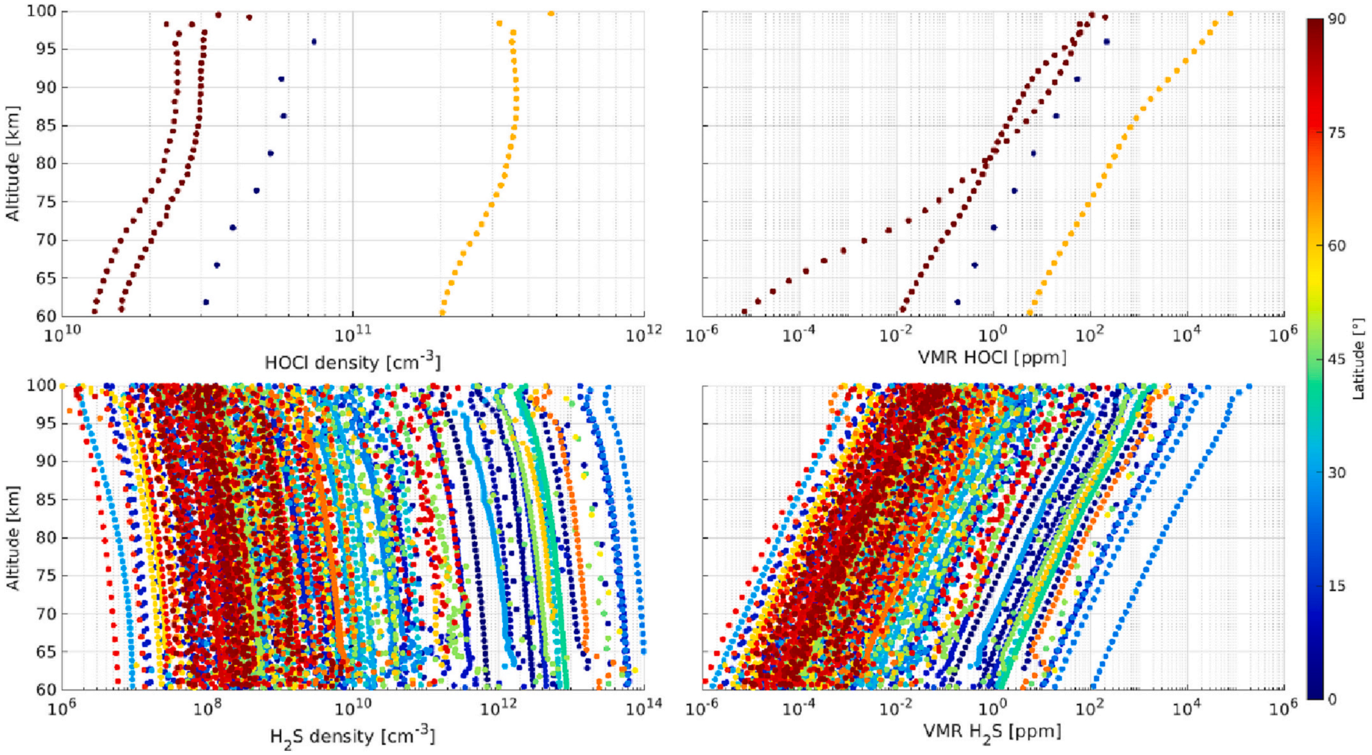

Fig. 19. Upper-limit number density profiles (left panels) and VMR profiles (right panels) of HOCl (top panels) and H_2S (bottom panels). The color code represents the absolute latitude of the observations.

5. Implications for Venus mesosphere climate and chemistry models

The updated SO_2, the new OCS, CS, CS_2, and SO_3 detections, and the H_2S and HOCl upper limit VMR profiles can be used to constrain Venus photochemical models and to better understand the sulfur chemistry above the cloud deck. The slightly increasing mean OCS VMR profile with altitude and its short photolysis lifetime (~6 h) suggest an upper mesosphere source for OCS not presently identified in models may be required. The detection frequency pattern for SO_3 suggests potential conversion between SO_3 and H_2SO_4 that might mean transport of sulfur to the upper mesosphere via condensed sulfuric acid is more viable as a source for the upper mesosphere SO_2 inversion layer than is implied by the upper limit on gas-phase H_2SO_4; analysis of the SO_2-SO_3-H_2SO_4 system and co-variations with temperature are needed to assess. The intermittent detections of CS in the mesosphere suggest there may be episodic injections or release from condensed phase of relatively reduced gases that have not been considered in recent modeling.

Despite caveats regarding decreased SOIR sensitivity to species abundances at higher altitudes – as the sensitivity decreases, the detectable limit increases – the newly reported SO_2, SO_3, CS, CS_2, and OCS detections motivate a need for a new paradigm in chemical modeling, Venus observing and Venus data analysis. For example, the detection of CS and the observed patterns in OCS detections are challenging. Chemically speaking CS, OCS, and CS_2 are linked via oxidation processing and photochemistry. Additionally, CS is highly reactive and has a short lifetime in general and especially within Venus conditions. CS reacting with metal-oxides leads to metal-sulfides. CS also reacts with concentrated H_2SO_4 producing CO, CO_2, SO_2, and N_2 gas products. CS polymerizes when left to its own devices in H_2SO_4-water solutions (Moltzen et al., 1988). Thus, the mere presence of the CS family of gases at Venus demands that chemical processing and sourcing at Venus be explored with new perspective.

The positive detections of the CS and CS_2 gases in the atmosphere motivate the need to determine the compatibility of the presence of these species with observations made at other wavelengths. To date, the UV absorption properties of CS gas have only been published at wavelengths below 170 nm. Occultations made with instrumentation paralleling the design of the BepiColombo PHEBUS instrument (Quémerais et al., 2020) or MAVEN IUVS instrument (McClintock et al., 2015) could be used to explore the CS vertical profile. Unfortunately, in spite of attempts made during the recent BepiColombo Venus flybys, due to technical difficulties, Venus stellar occultation observations were not obtained by BepiColombo and there are no other previously obtained Venus EUV occultation observations that may be used to explore the presence of CS in the Venus mesosphere. The availability of a EUV spectral instrument should be considered in the development of future Venus mission observation planning opportunities (via flybys or preferably using an asset in orbit at Venus).

The absorption response of CS_2 gas between 200 and 400 nm at temperatures ranging from 200 to 700 K has been explored and published (Grosch et al., 2015). These studies show that like SO_2, at UV wavelengths the CS_2 gas absorption cross-section is composed of highly structured electronic transitions located in two distinct bands. The first is located between 200 and 240 nm, while the second is located between 290 and 390 nm (Hearn and Joens, 1991). Currently, the only recent Venus observations with sufficient spectral resolution to unambiguously detect the structured CS_2 absorption lines present at UV wavelengths are the 2010 and 2011 Hubble data (Jessup et al., 2015). We find that these observations can tolerate CS_2 abundances of 10^{15} cm^{-3} (computed from the HST observations of Jessup et al. (2015)). Comparisons to the Na et al. (1994) rocket observations should also be considered in a future work. The values found in this work range from 10^{12} cm^{-3} at 70 km down to 4×10^{10} cm^{-3} at 95 km.

The Hubble data is unique in that it showed the temporally coincident and spatially co-located distribution of SO and SO_2 at 72 km based on UV observations. Submm observations, such as those obtained by ALMA and JCMT can also be used to retrieved co-located and temporally coincident SO and SO_2 measurements – however, these observations while sensitive to the 70–110 km altitude range, do not return a unique profile of the gases below 84 km. The Hubble observations showed unequivocally that the variations of SO and SO_2 that occurred relative to spatial location and Venus local time were not anti-correlated as would be predicted from direct sourcing of the SO gas from SO_2 photolysis. Instead, variations in the abundance of these as a function of latitude and Venus local time occurred in parallel, i.e., the SO increased as the SO_2 increased and vice versa. This behavior can only be supported if a third Venus reservoir exists. In other words, if the change in the SO abundance could have been predicted by the observed change in SO_2 we would have been able to conclude the two species were in equilibrium with each other. Since this was not observed, we are confident that a third reservoir exists. The submm observations show the same behavior is true in the upper mesosphere.

Equally intriguing is the fact that condensates produced by CS and CS_2 are brown, and so highly reflective near 600 nm which is a known property of Venus's yet to be identified cloud dwelling near UV-blue light absorbing species (Carlson, 2010; Jessup et al., 2020; Pérez-Hoyos et al., 2018). Notably, absorption created by the structured electronic transition lines of either CS_x gas would be incompatible with the smooth absorption pattern produced by the unknown absorber. However, formation of CS_x precipitate seems to be a natural chemical outcome when CS is in the presence of H_2SO_4-water solutions (Moltzen et al., 1988). Scattering off of the solid form of the CS_x species (if for example CS_x condensate is the nuclei of the H_2SO_4 haze) would lack highly structured absorption lines, yet remain strongly (albeit smoothly) absorbing in the UV. In fact, the smoothness of the absorption pattern produced by Venus's unidentified absorber suggests that the absorber is not a gas but some type of solid or aerosol (Titov et al., 2018).

If CS precipitate is a component of the unknown absorbing species chemical cycle, the photo-dependent production of that CS from CS_2 would suggest that the overall abundance of CS condensate may wane in the absence of sunlight and this could potentially lead to a different distribution of the species on the day and night sides. This is challenging, since it is known that the UV–visible absorption vertical profile collected by the Vega ISAV UV spectrometer between 54 and 10 km includes unidentified absorption shortward of 300 nm and unidentified absorption between 300 and 400 nm that does not directly parallel what is observed at the Venus cloud tops (Barker, 1979; Bertaux et al., 1996; Jessup et al., 2015). Could these discrepancies be a function not just of altitude variation in the unknown absorber, but the fact the ISAV profile was taken on Venus's nightside? The potential for CS or a compound made from CS to be linked to Venus's unknown absorber suggests this is a real possibility.

On the whole, the gas species newly detected by SOIR provide guidance about which additional chemical cycles should be more extensively explored when attempting to understand the chemical mechanics of Venus's atmosphere and what new chemical families (such as CS_x) need to be considered when modeling the past and current atmosphere All this raises questions such as: What is the linkage between OCS and SO_x? What influence does/can the potential episodic appearance of CS and CS_2 have on the overall sulfur budget? In what way is the unknown absorber chemistry linked to the sulfur species chemical cycle and dayside photolysis processes… if at all?

The SO_2 abundance is a few times larger than OCS in the mesosphere; furthermore, the SOIR results show that SO_2 is more readily detected (63.3% detection rate per orbit) than OCS (26.8% detection per orbit), see the summary in Table 3. The SOIR observations provides measurements of mesospheric CS, CS_2, and SO_3 which are important as they were never reported before. However, to know what it means in terms of the sulfur reservoir we would need to compare the ratio of SO_3, OCS, and CS to SO_2 on the same dates and locations on which each species was detected. To begin with, we already know that the SO_3 and CS species were detected only 19.6% and 12.3% of the time, while SO_2 was detected 63.3% of the time it was targeted (this assessment is only partially true because the detection limits for SO_2 and OCS are not always the same, i.e. for every occultation, every altitude). Since CS and SO_2 are almost always targeted together (as they have spectral signature in the same orders, 111 and 112, see Table 1, but with different detection limits, as their absorption lines have different intensities), this lets us know that the availability of the CS species at the abundance level required for detection is less stable than that of SO_2. However, we cannot make comment about the global reservoir without knowing how the gases behave coincidently through time. A first possible explanation would be that it is likely that when SO_2 spikes then the CS and SO_3 species are more readily detectable. This hypothesis could be verified by taking the ratio of CS/SO_2 and SO_3/SO_2 as well as mapping the $CS:SO_3:SO_2$ relative abundance for the dates when they were all detected. This will be done in a coming paper, as it falls beyond the scope of the present work.

Table 3
Detection rate per orbit and per spectrum of the different species.

Species	# of orbits targeting the species	Detection rate per orbit	# of spectra targeting the species	Detection rate per spectrum
SO_2	244	63.3%	8532	8.8%
SO_3	51	19.6%	1104	2.7%
CS	244	12.3%	1827	3.4%
CS_2	25	24%	528	2.7%
OCS	157	26.8%	6646	2.7%
HOCl	4	0%	136	0%
H_2S	213	0%	12,005	0%

6. Conclusions

Based on the 8-year database acquired in the Venus terminator region by the SOIR instrument on board Venus Express, we provide robust detections of SO_2, SO_3, CS, CS_2, and OCS above the cloud deck and upper limit volume mixing ratio values for H_2S and HOCl. The SO_2 profiles are an update to those published in Mahieux et al. (2015b). Comparison with the available values in the literature shows very good agreement of the retrieved profiles for SO_2 and reasonable agreement for OCS. The compatibility of the SOIR SO_3 detections with previous non-detections of gas-phase H_2SO_4 remains to be established. It is important to note the detections for all of these species may be biased to higher VMRs at higher altitudes based on the detection limits for SOIR. Detection fractions below ~30% (OCS, SO_3, and CS), may be an indication that $^2/_3$ of the time the VMR value of those species is below the SOIR detection threshold, however for $^1/_3$ of the time the species become detectable by SOIR during periods of localized (temporal and/or spatial) enhancements due to any number of factors including variability in the 3D transport mechanisms.

The SO_2 detections show a constant VMR between ~70 km and 90 km, around ~0.02 ppm, increasing at higher altitudes up to ~5 ppm at 100 km. We observe a time dependence of the detection with numerous detections at the beginning of the mission (Venus years 0 to 2), followed by a decrease. We do not observe a latitude or side of the terminator detection dependence.

The OCS detections show a increasing VMR with altitude with values ranging from ~5 ppb at 70 km up to ~1 ppm at 100 km. We do not observe a time dependence on the OCS detections, except for an increase in years 6 to 8 (more than a factor 3) while spatially we observe a decrease of detections in the 0°-30° latitude region. We do not observe a significant side of the terminator dependence.

The SO_3 detections show an increasing VMR between 75 km and 95 km, from ~0.1 ppm to ~20 ppm. The detection statistics of SO_3 show a different pattern than the one of SO_2, with sporadic larger detections. More detections are reported at mid-latitudes, and a significant difference between detections on the morning or evening sides is reported, with detections on the morning side at least double the rate on the evening side.

The CS detections show a constant VMR between 70 and 85 km, around ~0.2 ppm, followed by an increase up to 100 km with values up to 40 to 60 ppm. There might be a similar time dependency of the detections to the SO_2 detections, with the detection rate diminishing over time, except over years 0–2 and 4–6 which show lower detections than the general trend, a possible latitude dependence with more detections in the 60° to 70° and 70° to 80° latitude bins and fewer detections in the 0–30°, 30°-60°, and 80°-90° latitude bins, and no side of the terminator dependency.

CS_2 VMRs also increase with altitude, from values around ~0.02 ppm at 75 km increasing to ~6 ppm at 92 km. The detection statistics of CS_2 only cover years 2–6 of the mission, as no spectra covering the CS_2 bands were measured before or afterwards. Temporally, they are constant over years 2 to 6. In terms of latitude, the observations and detections are reported only in the sub-polar region and are constant over 70°-90°. In terms of local solar time, we see a clear difference with detections only on the morning side and no detection on the evening side.

H_2S and HOCl could not be detected, and upper limit profiles are provided.

Declaration of Competing Interest

The authors declare that they have no known competing financial interests or personal relationships that could have appeared to influence the work reported in this paper.

Data availability

Data will be made available on request.

Acknowledgments

*V*enus Express is a planetary mission from the European Space Agency (ESA). We wish to thank all ESA members who participated in the mission, in particular, H. Svedhem and D. Titov. We thank our collaborators at IASB-BIRA (Belgium), Latmos (France), and IKI (Russia), and in particular Dr. D. Fussen, who helped with some statistics aspects. We also would like to thank the anonymous Reviewers of this work for their valuable contributions. The research program was supported by the Belgian Federal Science Policy Office and the European Space Agency (ESA, PRODEX program, contracts C 90268, 90113, 17645, 90323, and 4000107727). A. Mahieux was supported by the Marie Skłodowska-Curie Action from the European Commission under grant number 838587. S. Robert thanks BELSPO for the FED-tWIN funding (Prf-2019-077 - RT-MOLEXO). F Mills was supported by NASA grant NNX16AN03G to SSI and by the University of Texas at Austin Center for Planetary Systems Habitability.

Appendix A. Supplementary data

Supplementary data to this article can be found online at https://doi.org/10.1016/j.icarus.2023.115556.

References

Arney, G., Meadows, V., Crisp, D., Schmidt, S.J., Bailey, J., Robinson, T., 2014. Spatially resolved measurements of H_2O, HCl, CO, OCS, SO_2, cloud opacity, and acid concentration in the Venus near-infrared spectral windows. J. Geophys. Res.: Planets. 119, 1860–1891.

Bains, W., et al., 2021. Phosphine on Venus cannot be explained by conventional processes. Astrobiology. 21, 1277–1304.

Baker, E.S., 1978. Detection of SO_2 and possibly CS_2 in the uv spectrum of Venus. In: Society, A.A. (Ed.), Division for Planetary Science. Pasadena, CA.

Barker, E.S., 1979. Detection of SO_2 in the UV Spectrum of Venus. Geophys. Res. Lett. 6, 117–120.

Belyaev, D., et al., 2012. Vertical profiling of SO_2 and SO above Venus' clouds by SPICAV/SOIR solar occultations. Icarus. 217, 740–751.

Belyaev, D.A., et al., 2017. Night side distribution of SO_2 content in Venus' upper mesosphere. Icarus. 294, 58–71.

Bertaux, J.L., Widemann, T., Hauchecorne, A., Moroz, V.I., Ekonomov, A.P., 1996. VEGA 1 and VEGA 2 entry probes: an investigation of local UV absorption (220-400 nm) in the atmosphere of Venus (SO_2, aerosols, cloud structure). J. Geophys. Res. 101, 12709–12746.

Bierson, C.J., Zhang, X., 2020. Chemical cycling in the Venusian atmosphere: a full photochemical model from the surface to 110 km. J. Geophys. Res.: Planets. 125 e2019JE006159.

Carlson, R., 2010. Venus' ultraviolet absorber and sulfuric acid droplets. In: International Venus Conference, Aussois, France, p. 4.

Chamberlain, S., et al., 2020. SOIR/VEx observations of water vapor at the terminator in the Venus mesosphere. Icarus. 346, 113819.

Colman, J.J., Xu, X., Thiemens, M.H., Trogler, W.C., 1996. Photopolymerization and mass-independent sulfur isotope fractionations in carbon disulfide. Science. 273, 774–776.

Domagal-Goldman, S.D., Meadows, V.S., Claire, M.W., Kasting, J., 2011. Using biogenic sulfur gases as remotely detectable biosignatures on anoxic planets. Astrobiology. 11, 419–441.

Encrenaz, P., et al., 2012. HDO and SO_2 thermal mapping on Venus: evidence for strong SO_2 variability. Astron. Astrophys. 543.

Encrenaz, T., Moreno, R., Moullet, A., Lellouch, E., Fouchet, T., 2015. Submillimeter mapping of mesospheric minor species on Venus with ALMA. Planet. Space Sci. 113-114, 275–291.

Encrenaz, T., et al., 2016. HDO and SO_2 thermal mapping on Venus. Astron. Astrophys. 595, A74.

Esposito, L.W., Copley, M., Eckert, R., Gates, L., Stewart, A.I.F., Worden, H., 1988. Sulfur dioxide at the Venus cloud tops, 1978–1986. J. Geophys. Res. 93, 5267–5276.

Esposito, L.W., Bertaux, J.L., Krasnopolsky, V., Moroz, V.I., Zasova, L.V., 1997. Chemistry of lower atmosphere and clouds. In: Bougher, S.W., Hunten, D.M., Phillips, R.J. (Eds.), Venus II: Geology, Geophysics, Atmosphere, and Solar Wind Environment. Univ. of Arizona Press, pp. 415–458.

Evdokimova, D., et al., 2021. The spatial and temporal distribution of nighttime ozone and sulfur dioxide in the Venus mesosphere as deduced from SPICAV UV stellar Occultations. J. Geophys. Res. Planets 126 e2020JE006625.

Gordon, I.E., et al., 2017. The HITRAN2016 molecular spectroscopic database. J. Quant. Spectrosc. Radiat. Transf. 203, 3–69.

Gröller, H., et al., 2018. MAVEN/IUVS stellar occultation measurements of Mars atmospheric structure and composition. J. Geophys. Res.: Planets. 123, 1449–1483.

Grosch, H., Fateev, A., Clausen, S., 2015. UV absorption cross-sections of selected sulfur-containing compounds at temperatures up to 500 °C. J. Quant. Spectrosc. Radiat. Transf. 154, 28–34.

Hearn, C.H., Joens, J.A., 1991. The near UV absorption spectrum of CS_2 and SO_2 at 300 K. J. Quant. Spectrosc. Radiat. Transf. 45, 69–75.

Jessup, K.L., et al., 2015. Coordinated Hubble space telescope and Venus express observations of Venus' upper cloud deck. Icarus. 258, 309–336.

Jessup, K.-L., Marcq, E., Bertaux, J.-L., Mills, F.P., Limaye, S., Roman, A., 2020. On Venus' cloud top chemistry, convective activity and topography: a perspective from HST. Icarus. 335, 113372.

Keating, G., et al., 1985. Models of Venus neutral upper atmosphere : structure and composition. Adv. Space Res. 5, 117–171.

Kettle, A.J., Kuhn, U., von Hobe, M., Kesselmeier, J., Andreae, M.O., 2002. Global budget of atmospheric carbonyl sulfide: temporal and spatial variations of the dominant sources and sinks. J. Geophys. Res.-Atmos. 107. ACH 25-1-ACH 25-16.

Krasnopolsky, V., 2010. Spatially-resolved high-resolution spectroscopy of Venus 2. Variations of HDO, OCS, and SO_2 at the cloud tops. Icarus. 209, 314–322.

Krasnopolsky, V., Pollack, J.B., 1994. H2O-H2SO4 system in Venus' clouds and OCS, CO and H_2SO_4 profiles in Venus troposphere. Icarus. 109, 58–78.

Krasnopolsky, V.A., 2008. High-resolution spectroscopy of Venus: detection of OCS, upper limit to H2S, and latitudinal variations of CO and HF in the upper cloud layer. Icarus. 197, 377–385.

Krasnopolsky, V.A., 2012. A photochemical model for the Venus atmosphere at 47-112 km. Icarus. 218, 230–246.

Krasnopolsky, V.A., 2016. Sulfur aerosol in the clouds of Venus. Icarus. 274, 33–36.

Lyons, J.R., 2009. Atmospherically-derived mass-independent sulfur isotope signatures, and incorporation into sediments. Chem. Geol. 267, 164–174.

Mahieux, A., et al., 2008. In-flight performance and calibration of SPICAV/SOIR onboard Venus express. Appl. Opt. 47, 2252–2265.

Mahieux, A., Wilquet, V., Drummond, R., Belyaev, D., Fedorova, A., Vandaele, A.C., 2009. A new method for determining the transfer function of an Acousto optical tunable filter. Opt. Express 17, 2005–2014.

Mahieux, A., et al., 2010. Densities and temperatures in the Venus mesosphere and lower thermosphere retrieved from SOIR onboard Venus express: retrieval technique. J. Geophys. Res. 115.

Mahieux, A., et al., 2015a. Update of the Venus density and temperature profiles at high altitude measured by SOIR on board Venus express. Planet. Space Sci. 113-114, 309–320.

Mahieux, A., et al., 2015b. Venus mesospheric sulfur dioxide measurement retrieved from SOIR on board Venus express. Planet. Space Sci. 113-114, 193–204.

Mahieux, A., et al., 2015c. Rotational temperatures of Venus upper atmosphere as measured by SOIR on board Venus express. Planet. Space Sci. 113-114, 347–358.

Mahieux, A., Wilquet, V., Vandaele, A.C., Robert, S., Drummond, R., Bertaux, J.L., 2015d. Hydrogen halides measurements in the Venus upper atmosphere retrieved from SOIR on board Venus express. Planet. Space Sci. 113-114, 264–274.

Marcq, E., Bézard, B., Encrenaz, T., Birlan, M., 2005. Latitudinal variations of CO and OCS in the lower atmosphere of Venus from near-infrared nightside spectro-imaging. Icarus. 179, 375–386.

Marcq, E., Bézard, B., Drossart, P., Piccioni, G., Reess, J.M., Henry, F., 2008. A latitudinal survey of CO, OCS, H_2O, and SO_2 in the lower atmosphere of Venus: spectroscopic studies using VIRTIS-H. J. Geophys. Res. 113 https://doi.org/10.1029/2008JE003074.

Marcq, E., et al., 2011. An investigation of the SO_2 content of the venusian mesosphere using SPICAV-UV in nadir mode. Icarus. 211, 58–69.

Marcq, E., Bertaux, J.L., Montmessin, F., Belyaev, D., 2013. Variations of Sulphur dioxide at the cloud top of Venus's dynamic atmosphere. Nat. Geosci. 6, 25–28.

Marcq, E., Mills, F.P., Parkinson, C.D., Vandaele, A.C., 2018. Composition and chemistry of the neutral atmosphere of Venus. Space Sci. Rev. 214 article 10.

Marcq, E., et al., 2020. Climatology of SO_2 and UV absorber at Venus' cloud top from SPICAV-UV nadir dataset. Icarus. 335.

McClintock, W.E., et al., 2015. The imaging ultraviolet spectrograph (IUVS) for the MAVEN Mission. Space Sci. Rev. 195, 75–124.

Mills, F.P., Allen, M., 2007. A review of selected issues concerning the chemistry in Venus' middle atmosphere. Planet. Space Sci. 55, 1729–1740.

Moltzen, E.K., Klabunde, K.J., Senning, A., 1988. Carbon monosulfide: a review. Chem. Rev. 88, 391–406.

Moroz, V.I., et al., 1990. Water vapor and sulfur dioxide abundances at the Venus cloud tops from the Venera-15 infrared spectrometry data. Adv. Space Res. 10, 77–81.

Moses, J.I., Allen, M., Gladstone, G.R., 1995. Post-SL9 sulfur photochemistry on Jupiter. Geophys. Res. Lett. 22, 1597–1600.

Na, C.Y., Esposito, L., McClintock, W.E., Barth, C.A., 1994. Sulfur dioxide in the atmosphere of Venus: II. Modeling results. Icarus. 112, 389–395.

Nevejans, D., et al., 2006. Compact high-resolution space-borne echelle grating spectrometer with AOTF based on order sorting for the infrared domain from 2.2 to 4.3 micrometer. Appl. Opt. 45, 5191–5206.

Oschlisniok, J., et al., 2021. Sulfuric acid vapor and sulfur dioxide in the atmosphere of Venus as observed by the Venus express radio science experiment VeRa. Icarus. 362, 114405.

Pérez-Hoyos, S., et al., 2018. Venus upper clouds and the UV absorber from MESSENGER/MASCS observations. J. Geophys. Res.: Planets. 123, 145–162.

Piccialli, A., Moreno, R., Encrenaz, T., Fouchet, T., Lellouch, E., Widemann, T., 2017. Mapping the thermal structure and minor species of Venus mesosphere with ALMA submillimeter observations. Astronomy & Astrophyics 606, A53.

Piccialli, A., et al., 2021. Impact of gradients at the martian terminator on the retrieval of ozone from SPICAM/MEx. Icarus. 353, 113598.

Pinto, J.P., et al., 2021. Sulfur monoxide dimer chemistry as a possible source of polysulfur in the upper atmosphere of Venus. Nat. Commun. 12, 175.

Prinn, R.G., 1975. Venus: chemical and dynamical processes in the stratosphere and mesosphere. J. Atmos. Sci. 32, 1237–1247.

Quémerais, E., et al., 2020. PHEBUS on Bepi-Colombo: post-launch update and instrument performance. Space Sci. Rev. 216, 67.

Sandor, B., Clancy, R.T., Moriarty-Schieven, G., 2012. Upper limits for H_2SO_4 in the mesosphere of Venus. Icarus. 217, 839–844.

Sandor, B.J., Clancy, R.T., Moriarty-Schieven, G., Mills, F.P., 2010. Sulfur chemistry in the Venus mesosphere from SO_2 and SO microwave spectra. Icarus. 208, 49–60.

Sonnabend, G., et al., 2005. A new search for OCS in the middle atmosphere of Venus. AAS DPS Meet. 37.

Titov, D.V., Ignatiev, N.I., McGouldrick, K., Wilquet, V., Wilson, C.F., 2018. Clouds and hazes of Venus. Space Sci. Rev. 214, 1–61.

Trompet, L., et al., 2016. Improved algorithm for the transmittance estimation of spectra obtained with SOIR/Venus express. Appl. Opt. 55, 9275–9281.

Trompet, L., et al., 2022. Carbon dioxide retrievals from NOMAD-SO on ESA's ExoMars trace gas orbiter and temperature profiles retrievals with the hydrostatic equilibrium equation. I. Description of the method. J. Geophys. Res. Planets. 128 e2022JE007279.

Trompet, L., Robert, S., Mahieux, A., Schmidt, F., Erwin, J., Vandaele, A.C., 2021. Phosphine in Venus' atmosphere: detection attempts and upper limits above the cloud top assessed from the SOIR/VEx spectra. A&A. 645, L4.

Vandaele, A.C., et al., 2013. Improved calibration of SOIR/Venus express spectra. Opt. Express 21, 21148.

Vandaele, A.C., et al., 2017a. Sulfur dioxide in the Venus atmosphere: I. Vertical distribution and variability. Icarus. 295, 16–33.

Vandaele, A.C., et al., 2017b. Sulfur dioxide in the Venus atmosphere: II. Spatial and temporal variability. Icarus. 295, 1–15.

Wilquet, V., Drummond, R., Mahieux, A., Robert, S., Vandaele, A.C., Bertaux, J.L., 2012. Optical extinction due to aerosols in the upper haze of Venus: four years of SOIR/VEX observations from 2006 to 2010. Icarus. 217, 875–881.

Zasova, L.V., Moroz, V., Esposito, L., Na, C.Y., 1993. SO_2 in the middle atmosphere of Venus: IR measurements from Venera-15 and comparison to UV data. Icarus. 105, 92–109.

Zasova, L.V., Moroz, V.I., Linkin, V.M., Khatountsev, I.A., Maiorov, B.S., 2006. Structure of the Venusian atmosphere from surface up to 100 km. Cosm. Res. 44, 364–383.

Zhang, X., Liang, M., Mills, F., Belyaev, D., Yung, Y., 2012. Sulfur chemistry in the middle atmosphere of Venus. Icarus. 217, 714–739.